UiT The Arctic University of Norway

Faculty of Science and Technology
Department of Physics and Technology

A Study of Polarimetric Parameters Used for Sea Ice Classification

Ida G. Kinderås

EOM-3901 Master's thesis in energy, climate and environment Dec 2021

“Ice Ice Baby”
–Vanilla Ice

Acknowledgements

First and foremost, I would like to thank my supervisor, Malin Johansson for the guidance and support throughout this process, your advice and interesting discussions have been invaluable in writing this theses. I would also like to thank my co-supervisor, professor Torbjørn Eltoft for his theoretical inputs and contribution to the discussion. Another thank you to Dr. Martine Espeseth for the use of images and figures used in this thesis.

RADARSAT-2 data was provided by NSC/KSAT under the Norwegian-Canadian Radarsat agreement 2019.

To my friends and colleagues, thank you for the love, support and encouraging words during the writing of this thesis. To my brother, Jørgen thank you for your silent support, and for answering the phone (sometimes).

Lastly, a great thanks to my parents, not only for the support I have received during the process of writing this thesis, but for all the unconditional love and support I have always received. A special thanks to my mom for proofreading this thesis.

Ida G. Kinderås
Tromsø, December 2021

Abstract

The Arctic region of the Earth are largely covered by sea ice, which is important for the marine ecosystems locally in the region, but it also has an impact on the climate systems. Recent climate changes means that the sea ice is melting and the coverage is shrinking which can have a global impact. Monitoring these sea ice changes are important to get an understanding of this impact. There are multiple options for how to carry out this monitoring, but the Arctic is a cold, dark and remote region, so a good option is using satellite images. A special advantage of using SAR (Synthetic Aperture Radar) satellites is that they are insensitive to weather conditions and darkness, which can be a challenge in the Arctic regions, especially during the winter months. Today operational ice services produces sea ice charts using such SAR images but they primarily reply on dual-polarimetric data. These images covers large areas due to the large swath for these modes and are idea for a Pan-Arctic coverage. However, they are impacted by e.g., effects of varying incidence angle throughout the images. This thesis will study the possibilities that lies within radar polarimetry, a field that utilized fully polarimetric data to extract even more information regarding the target on the surface, in this case sea ice. Moreover, these images enabled extraction of scattering type information and through this added information improve the sea ice type classification maps. The images studied here are two sets of fully polarimetric RADARSAT-2 data that covers the same sea ice but with varying incidence angles. Four different polarimetric features; the co-polarization ratio, the M-parameter, degree of polarization as well as the polarimetric coherence, were investigated for their separability measures between different sea ice types as well as how affected they are by incidence angle variations. Out of these four the co-polarization ratio was found to be useful to separate the thinner sea ice types as well as open water from the surrounding thicker sea ice. Both the M-parameter and the degree of polarization showed promise in separating deformed sea ice from the other ice types at higher incidence angles. Though limited consistent separability between different ice types were observed for the polarimetric coherence. The polarimetric coherence was found to be independent on the incidence angle, though the other three parameters showed an incidence angle dependency.

Contents

List of Figures

List of Tables

1 Introduction

A large part of the Arctic region is covered by sea ice, and the sea ice in this regions is important for the climate on the Earth, as well as an important part of the marine ecosystems and gas exchanges through the opening of leads and deformation processes. Leads enable light and gas transfers, whereas ridges provide safe heavens for marine ecosystems. The sea ice extent is decreasing and combined with the reduced albedo will this have an impact globally, and the possibility to monitor and study the sea ice is therefor important. This thesis will investigate remote sensing of sea ice using synthetic aperture radar (SAR) satellites, and more specifically remote sensing of sea ice using fully polarimetric radar data. The introduction of this thesis will start with the motivation and reason for this work, before continuing with a brief overview of the state of the art. The research questions to be studied will also be presented. This chapter will also include the structure of the thesis and give a short summary of the upcoming chapters. Some of the work done in this thesis is preceding the work done in pilot project [Kinderaas, 2018].

1.1 Motivation and State of the Art

As mentioned the sea ice around the poles is an important part of the Earth's climate system, and due to the climate changes seen in the later years the sea ice is shrinking [Stroeve et al., 2012]. Not only is the seasonal sea ice cover decreasing in both thickness and extent, but the multiyear sea ice coverage is

also decreasing. A reduction in sea ice coverage will have an impact on the marine ecosystems in the Arctic, but can also possibly alter weather conditions and have an impact on the long time climate on earth. It is therefore important to have an understanding of the sea ice cover, both to monitor the impact on Earth's climate system, and also for the increased interest for commercial maritime activity in the Arctic regions [Stroeve et al., 2012] (and references therein).

Monitoring of sea ice can be a challenge. The Arctic regions are not the most welcoming when it comes to weather, temperature or daylight (during the winter months), in addition these regions are very remote and difficult to access. Sea ice is therefore operationally monitored using satellite images and in particular SAR images. By using satellites it is possible to monitor large areas daily, and as will be further explored in this thesis SAR satellites also eliminated the need for daylight and good weather conditions.

The operational ice services produce daily sea ice charts, out of which an example can be seen in Figure [1.1]. The sea ice charts created by operational ice services such as the Norwegian Meteorological Institute are produced using primarily SAR images, the work relies on satellite images but is largely done manually by sea ice experts. Improved understanding of the sea ice responses in the SAR images can therefore ultimately be used towards a more automatic system. The images used are dual-polarimetric images and have a large swath and covers a large area meaning that incidence angle effects can be observed across these images [Lohse et al., 2020]. Even with dual-polarimetric data it is possible to perform sea ice classification by separating different sea ice types e.g., [Lohse et al., 2020], and to differentiate between open water and sea ice, e.g., [Geldsetzer and Yackel, 2009]. In this thesis fully polarimetric data will be studied, this data have a smaller swath and are therefore less affected by incidence angle within the individual images. Using fully polarimetric data also provides the possibility to explore the scattering mechanisms and extract additional information from the ice.

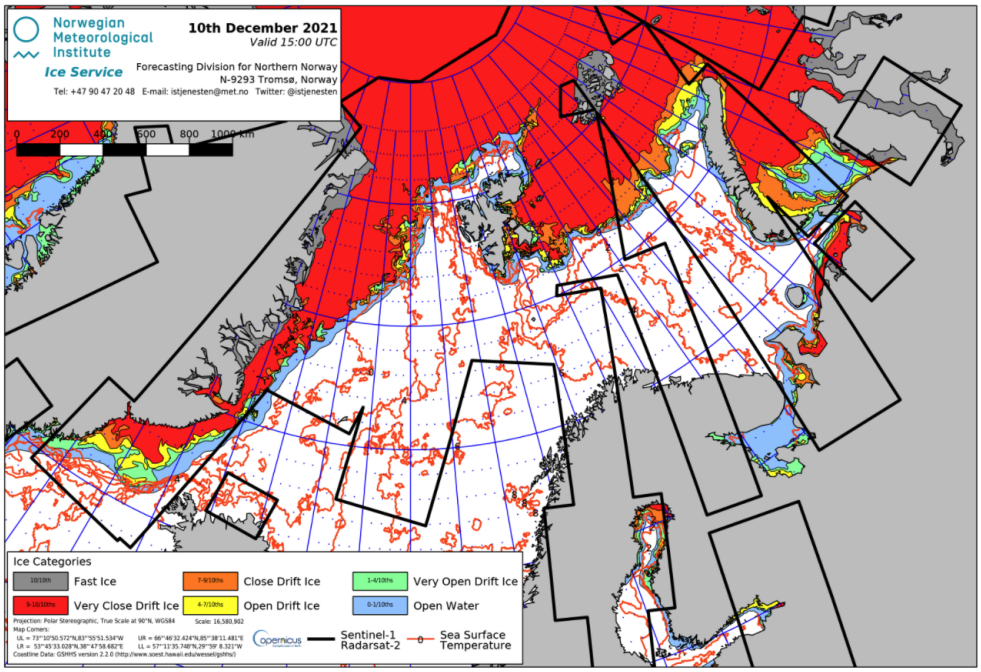

Figure 1.1: Sea ice chart created by the Norwegian Meteorological Institute on 10th of December 2021 [MET.no,].

The field of sea ice research is ever evolving, and studies by [Brekke et al., 2014], [Gill et al., 2013], [Drinkwater et al., 1992], [Geldsetzer and Yackel, 2009] among others have all been exploring the field of sea ice monitoring using fully polarimetric data. In [Gill et al., 2013] and [Drinkwater et al., 1992] different polarimetric parameters were used for sea ice classification. In [Gill et al., 2013] they made use of the co-polarization ratio (VV/HH) to separate the open water areas from the newly formed sea ice as well as from the thicker sea ice types. In this thesis four different polarimetric parameters and their responses to four different sea ice types as well as open water are investigated. For this SAR images covering an area just north of Svalbard are investigated consisting of predominantly newer sea ice, newly formed and young sea ice, as well as first and second year ice. At the time of the images used, December 2019, the newer sea ice was formed primarily in the leads. The new ice consists of both high and low backscatter areas, enable investigations into if the two different backscatter regimes can be separated using any of the four parameters investigated here.

1.2 Research Questions

The aim of this study is to investigate if fully polarimetric radar data can be utilized for monitoring sea ice development in the Arctic. This thesis will investigate a selection of polarimetric parameters to see if it is possible to provide even more information about the sea ice types.

The thesis will utilize fully polarimetric Radarsat-2 data that has been collected during the winter months, north of Svalbard. The images to be studied are collected withing a few hour from each other and with varying incidence angle. This provides the opportunity to study the same ice, but with different incidence angles. This thesis will therefor also focus on the affect the incidence have on the polarimetric parameters, and assess if this is something that must be considered when using these specific parameters.

In particular, this thesis will address two main research questions:

1. *Is it possible to use the polarimetric parameters studied in this thesis to determine sea ice type?*

2. *In the case of varying incidence angle, how does the parameters behave? Can the parameters be used without having to consider incidence angle?*

1.3 Structure of Thesis

A brief introduction to the content of each chapter in this thesis will be presented here.

Chapter 2 presents the the principles of sea ice, the different formation stages of sea ice and the different sea ice types. This chapter also gives an introduction to remote sending of sea ice.

Chapter 3 provides an introduction to the most important SAR principles, looking at the theory and physics related to SAR satellites.

Chapter 4 gives an introduction to radar polarimetry. It looks at the basic theory of the field as well as introducing some decomposition theorems.

Chapter 5 provides presentation of the data to be used in this thesis as well as defining the study area.

Chapter 6 addresses the methodology. It presents the polarimetric parameters to be used in this thesis, as well as an assessment of the data to be used.

Chapter 7 presents and discusses the results found in this thesis. The results for each polarimetric parameter are presented together with a discussion of said parameter.

Chapter 8 concludes the work done in this thesis and provides suggestions for some further work based on findings.

2

Sea Ice

In the polar regions a dominant feature to be found is sea ice. Sea ice cover around the poles are crucial for the climate all over the globe, and a change in this coverage could have a significant impact on the climate system. It is therefore very important to have an understanding of the function and physics of sea ice in order to have an even greater understanding of the climate changes we see today. Sea ice concentration, extent and type are regularly monitored by ice services around the world, and here satellite images play an important role. A thorough understanding of the sea ice signatures in satellite images are therefore essential.

2.1 Sea Ice Coverage

71 % of the Earth's surface is covered by water, and out of this area 7-15% is covered by sea ice. There is a range in the percentage due to the fact that the sea ice coverage will vary with different seasons, e.g., during the winter months there will be more sea ice present than it will be during the summer months. The total sea ice coverage of the Earth's surface is equivalent to 5-10%. In the Arctic region the sea ice minimum normally occurs in September and the sea ice maximum in March [Shokr and Sinha, 2015].

2.2 Different Types and the Formation of Sea Ice

There are several different stages of sea ice formation, and within these different formation stages several different types of sea ice is found. The World Meteorological Organization ([WMO, 2010]) have defined sea ice types in different stages of the development, these types are often used for classification purposes and are further described below. It is not always possible to observe all these types in SAR, but variation in surface roughness can be possible to observe, and work by [Isleifson et al., 2010] have shown how the normalized radar cross sections (NRCS) for VV, VH and HH in SAR images are changing during the early stages of sea ice growth.

2.2.1 Stage 1: less than 30 cm thick

In the first stage of sea ice development, the ice is less than 30 cm thick and it is where *frazil ice* begins to form in the ocean, and as the ocean continues to become colder, frazil ice merges together forming *grease ice*. The grease ice is formed under calm ocean surface conditions, with light winds and no waves. Further in this stage of sea ice formation the type of sea ice formation depends on several different variables, for example snow fall, the cooling rate of the sea ice formation, and also the salinity of the water. Examples of sea ice types that have different salinity levels are *ice rinds* and *nilas*. When the water has low salinity levels it can freeze into *brittle ice*, thin salt-free layers, forming ice rinds. Nilas are formed in water with high salinity levels, and a characteristic of nilas is its elastic properties that is a result of the fast freezing process. It is possible to divide nilas in to two categories based on its thickness; dark nilas (up to 5 cm thickness) and light nilas (up to 10 cm thickness) [WMO, 2010]. Figure [2.1] shows an example of nilas that have been formed in calm water.

In [Isleifson et al., 2010] they show that for the co-polarized NRCS the lowest backscatter values are observed for grease ice. This is believed to be caused by grease ice having a low dielectric constant. Further there is observed an increase in backscatter values when observing nilas, dark-nilas and light-nilas, where the light nilas has the highest relative backscatter. As the ice thickens and the light-nilas are formed there will be a higher presence of volume scattering, which again result in the increase in NRCS [Isleifson et al., 2010].

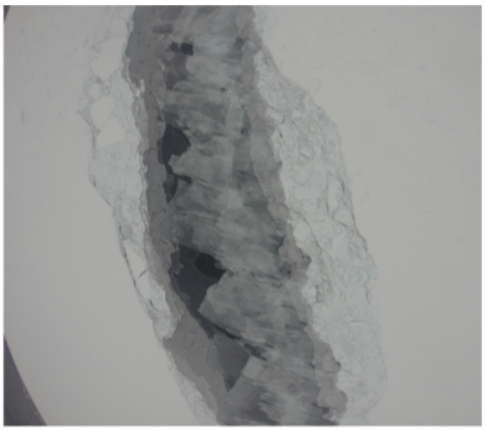

Figure 2.1: Photo of nilas formed in calm waters. Photo used with permission of Dr. Martine Espeseth.

As the different types of ice continues to freeze it will become thicker, and at 10-15 cm thickness it is called *grey-ice*. When the ice is reaching a thickness up to 30 cm it is called *grey-white ice*. All sea ice types that is collected under this stage of the formation process can be referred to as *young ice*. Young ice is sensitive to the exposure of rough weather conditions and can be broken up to smaller parts [WMO, 2010]. Ice formation often occur in leads within the pack ice during the freeze-up and winter time period.

2.2.2 Stage 2: 30 cm - 2 m thick

The second stage of sea ice formation is often known as first-year ice (FYI). It is possible to further divide first year ice into subcategories based on the thickness. The different categories of first year ice can be seen in table [2.1] [WMO, 2010].

Table 2.1: Table describing subcategories of first year ice [WMO, 2010]

First year subtype	Ice thickness
Thin first-year ice	30-70 cm
Medium first-year ice	70-120 cm
Thick first-year ice	120-200 cm

2.2.3 Stage 3: Second year- and Multiyear Ice

When the ice survives its first year of formation it is often referred to as second year ice, and as the ice continues to survive over multiple years it is referred to as multiyear ice. Each season when the ice reaches sea ice minimum the formation stages starts up again, and processes seen in stage one and two will occur again. In this formation stage the sea ice is often in the range of 1.2-4 m thick, depending on the melt, growth and ridging during seasons the thickness can vary [WMO, 2010].

Multi-year ice will have a smoother top-surface than second-year ice, one of the reasons for this is the lower salinity in the ice as a result of brine drainage during summer melt period [WMO, 2010]. The brine drainage result in a lower salinity content of the ice, and air bubbles formed in the ice can lead to more volume scattering.

2.2.4 Deformation of Sea Ice

Deformation of sea ice occur when the ice is subjected to pressure. In cases where the ice is thin, e.g. young ice, the subjected pressure may result in rafting and for thicker ice ridging can occur. Ridges are formed when ice is lifted up and piled up over the existing sea ice levels. Some areas of the ice are also being pressed down in order to support the overlying ice during this deformation, it is possible to call the underlying ice Keel. The height of the ridges ranges between 5 and 30 meters [Leppäranta, 2011]. Ridged and rafted areas are easily observable in SAR images due to their high backscatter values and strong signal in the HV channel [WMO, 2010]. Figure [2.2] is showing photos of different sea ice types acquired in the Barents Sea during the N-ICE project managed by the Norwegian Polar Institute.

Ridges
Photographs courtesy Martine Espeseth, N-ICE 2015, Norweigan Polar Institute, Date: May 2015

Grey-white ice covered with 2-3 cm of snow (removed manually on the lower corner of the photo)
Photographs courtesy Martine Espeseth, N-ICE 2015, Norweigan Polar Institute, Date: May 2015

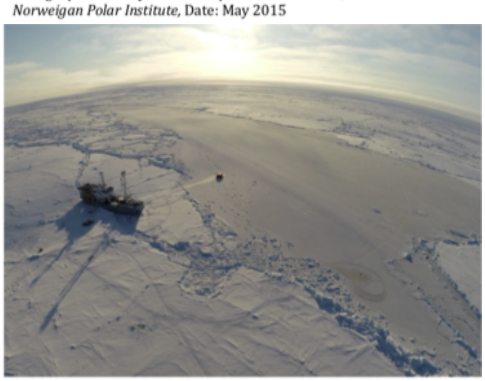

Multi-year ice (left corner) and newly formed ice (right side of the photo)
Photographs courtesy Sebastian Sikora, UNIS, N-ICE 2015, Norweigan Polar Institute, Date: May 2015

Figure 2.2: Photos showing different sea ice types (Used with permission of Dr. Martine Espeseth)

2.3 Remote Sensing of Sea Ice

As mentioned in the introduction, the backscatter signatures from sea ice are often complex, and it is therefore important to be able to understand and utilize the properties and the physical processes of the ice when looking at the microwave signature. Sea ice research is a continuous work, and the field of remote sensing of sea ice is still under development. One of the reasons that the backscatter signature of the sea ice is such a complex process is the fact that the sea ice surface is in constant change and development. Sea ice can be at looked as a heterogeneous media [Lubin and Massom, 2006].

In order to understand the changes in the sea ice backscatter signatures it is primarily important to understand the physical processes and the properties of the sea ice, and its interactions with microwaves. The backscattered signal from the ground target is a function of the frequency, incidence angel and polarization, these satellite image properties will be further discussed in Sections 3 and 4. A lower frequency enables a longer penetration depth and multi-polarization ensures that more information about the scattering mechanisms can be retrieved, whereas the incidence angle dependency means that with higher incidence angle the backscatter signature is lower.

Examples of physical properties of the sea ice that will affect the backscatter signature is the brine and air content of the ice, the crystal structure, the surface roughness properties and the dielectric properties [Tucker III et al., 1992].

The heterogenity and very complex structure of sea ice is reflected in the dielectric constant of sea ice. It can be said that sea ice is built up of three phases, there is the liquid brine, air and the pure ice. This will result in the dielectric constant being determined by different factors, as for example, the density of the ice, the brine volume, and also the dielectric properties of the brine and the ice itself. The dielectric properties are summarised in the complex dielectric constant, ϵ. By knowing this key parameter, it is possible to interpret the propagation of the electromagnetic wave. It is also possible to determine the scattering and reflection of the electromagnetic wave by the dielectric constant. The dielectric constant is defined in equation [2.1] [Lubin and Massom, 2006].

$$\epsilon^* = \epsilon_0(\epsilon' - j\epsilon'') \tag{2.1}$$

By this definition the dielectric constant is looked at as a complex number, where ϵ_0 is defined as the free-space dielectric constant, while ϵ' and ϵ'' is referring to the real and the imaginary parts, respectively. It is also possible

to refer to ϵ' as the relative permittivity and ϵ'' as the dielectric loss factor [Lubin and Massom, 2006].

3

Synthetic Aperture Radar (SAR)

Synthetic Aperture Radar (SAR) is an imaging system that is commonly used in remote sensing. This chapter will give an introduction to the basic principles of SAR and provide an explanation of limitations and difficulties that can be met using Synthetic Aperture Radar in remote sensing.

3.1 Introduction to SAR

SAR is an active imaging system that is transmitting electromagnetic radiation in the microwave region of the electromagnetic spectrum. The microwave region of the electromagnetic spectrum is located at wavelengths between 1 mm to 30 cm. Table [3.1] describes the most commonly used wavelengths for radar imaging.

Table 3.1: Most commonly used wavelength and frequency bands in radar remote sensing (based on [IEE, 2003])

Band	Wavelength (cm)	Frequency (GHz)
VHF	100-1000	0.03-0.3
UHF	30-100	0.3-1
L	15-30	1-2
S	7.5-15	2-4
C	3.75-7.5	4-8
X	2.5-3.75	8-12
Ku	1.67-2.5	12-18
K	1.11-1.67	18-27
Ka	0.75-1.11	27-40

The imaging SAR system is mounted on a moving platform like an airplane or a satellite and it operates a side-looking geometry. When the SAR system illuminates the Earth's surface it does so perpendicular to the flight direction [Lee and Pottier, 2009].

SAR sensors works in a way that the system will transmit a microwave pulse that illuminates the Earth's surface and the same system will collect the electromagnetic signal that is scattered from the surface and back to the sensor. The signal that is scattered back to the sensor is often referred to as backscatter, and depending on the geometry of the surface that is illuminated the backscatter will have different properties [Lee and Pottier, 2009].

One of the greatest advantages of SAR sensors is that it is an active system, meaning the system is capable of transmitting its own signal and can therefore acquire images all hours of the day. It is not dependent of solar illumination, and will therefore be able to gather images even during the dark polar nights. Another great advantage with SAR technology is that since the system is operating within the microwave region of the electromagnetic spectrum it will be less affected by weather conditions like clouds, rain or other atmospheric attenuation's. This results in the SAR sensor being able to provide imaging of the Earth's surface 24 hours of the day and under almost any weather conditions (different wavelengths may react differently to atmospheric conditions) [Lee and Pottier, 2009].

3.2 The Radar Equation

The equation that describes the interaction between an electromagnetic wave and a given target is referred to as the radar equation [3.1], and is an important equation to understand the mechanisms behind radar sensors. When an electromagnetic wave interacts with a target on the surface it is possible to observe a change in the electromagnetic energy returning to the sensor/receiver. The reason for the change in the returning energy is that when energy is hitting a target on the surface some of this energy is absorbed by the target itself before it is re-radiated as a new electromagnetic wave back to the receiver. This is interesting as the change in the electromagnetic energy might be useful when identifying the target on the surface. One thing that is particularly interesting is the changes regarding the polarization of the wave [Lee and Pottier, 2009].

The radar equation is given as:

$$P_r = \frac{P_T G_T(\theta,\phi)}{4\pi r_T^2}\sigma\frac{A_{ER}(\theta,\phi)}{4\pi r_R^2} \tag{3.1}$$

Here P_r is the power that is detected by the receiver, P_T is the transmitted power, G_T is the transmitting antenna gain, A_{ER} is the receiving antennas effective aperture, r_T is the distance from the transmitting system to the target, r_R is the distance from the target to the receiving system, and θ and ϕ are spherical angles that are defining the direction of observations [Lee and Pottier, 2009].

The variable σ in the radar equation [3.1] is referred to as the radar cross section and it is given by:

$$\sigma = 4\pi r^2 \frac{|\overrightarrow{E_S}|^2}{|\overrightarrow{E_I}|^2} \tag{3.2}$$

Where E_I is the incident (wave or field)) and E_S is the scattered wave/field. The radar cross section presented in equation [3.2] contains information related to the target on the ground.

3.3 Radar Geometry

As mentioned earlier, the SAR imaging system is an active system, meaning that it consists of a antenna that is able to both transmit a pulsed microwave signal, as well as to receive the recorded backscatter from the surface. The mentioned side-looking geometry of a SAR sensor can be seen in Figure [3.1]. The direction that the system is travelling, is often referred to as the azimuth direction, or the along-track direction(y-direction). The direction of the antenna beam, or the direction the system in "looking" is often referred to as the range direction or the cross-track direction(x-direction) [Lee and Pottier, 2009]. The slant range is referred to the path that the signal travels from the aircraft to the ground [van Zyl and Kim, 2011]. The geometry of a SAR system with side-looking geometry is illustrated in Figure 3.1.

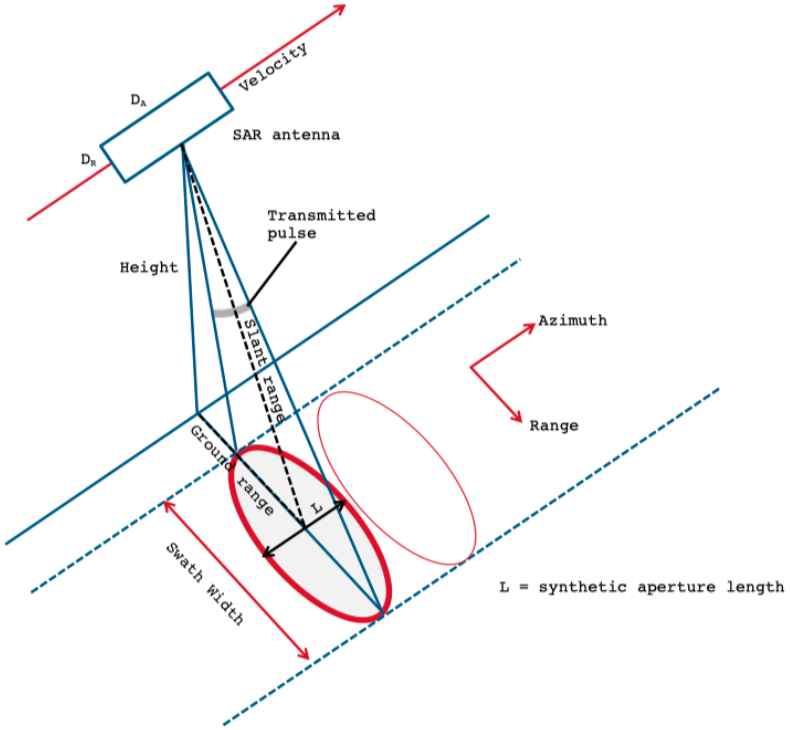

Figure 3.1: SAR imaging geometry (Figure used with permission of Dr. Martine Espeseth)

As seen in Figure 3.1, the area on the ground that is being scanned by the antenna beam is called Radar swath, and the area that is within the beam at a given time is the antenna footprint.

3.4 SAR Resolution

The resolution of an image can be defined as the smallest distance between two targets in the image that still can be resolved.[van Zyl and Kim, 2011]. In radar imaging systems it is normal to differentiate between two different types of resolution, range and azimuth resolution.

3.4.1 Range Resolution

The range resolution can be based on the time and the distance of the radar wave. When the radar wave propagates it will move at the speed of light, and it is possible to measure the time difference between the corresponding echoes. This time difference can be defined as [van Zyl and Kim, 2011]:

$$\Delta t = 2x_r/c \tag{3.3}$$

Here x_r is defined as the slant range direction that is separating two point targets, c is the speed of light, and the number 2 is there to take into account that the signal is travelling the distance two times, down from the sensor and then back up again. It is further possible to define the smallest difference that is separable by the radar receiver as the effective time length τ of the pulse. It is then possible to rewrite equation 3.3 and solve for x_r in order to define the slant range resolution [van Zyl and Kim, 2011]:

$$2x_r/c)\tau \rightarrow x_r = \frac{c\tau}{2} \tag{3.4}$$

It is possible to "transform" the slant range resolution into ground range resolution, x_g, by also taking into account the the incident angle:

$$2x_g sin\theta/c = \tau \rightarrow x_g = \frac{c\tau}{2sin\theta} \tag{3.5}$$

The equations above describe the situation for a pulsed radar system, with no pulse coding. The range resolution in equation [3.5] is limited by the pulse length. It is technically difficult to generate pulses that are very short. To increase the range resolution, SAR sensors use coding of the pulse, i.e. a 'chirped' pulse, which is a long pulse with a linear frequency modulation. If the pulse is not frequency modulated the smallest possible distance that can exist between two targets which can be separated, needs to be $c\tau/2$. Using a chirped signal, this resolution is determined by the inverse of the actual pulse bandwidth, and can in fact be down to a few meters [Johannessen et al.,].

It is important to note that the ground range resolution is dependent on the incident angle, and will vary throughout the image.

3.4.2 Azimuth Resolution

The azimuth resolution of a SAR radar can be defined as half the size of the size of the physical antenna. One special characteristic of the SAR azimuth resolution is that it is not dependent on the distance between the sensor and the surface [van Zyl and Kim, 2011]. In order to achieve high resolution in azimuth would require a physically large antenna, a problem that is solved in SAR by "synthesizing " the aperture. The expression for the SAR azimuth resolution is given by [Lee and Pottier, 2009].

$$x_a = \frac{L}{2} \tag{3.6}$$

Another interesting fact about the azimuth resolution is that it is also independent of the wavelength of the wave.

3.5 SAR Microwave Bands

A radar system is operating within a given portion of the electromagnetic spectrum, the region which is referred to as the microwave region. The microwave region of the electromagnetic spectrum is defined to be ranging between 1 mm to 30 cm in wavelength. The region stretches over a large range of wavelengths, and it is therefore also possible to divide the region into smaller sub-regions. These sub-regions are often referred to as microwave bands [Campbell, 2011] and are presented in Table 3.1. The choice of band will have an impact on the resulting radar image, for example penetration depth will vary depending on wavelength. Longer wavelengths will have a deeper penetration depth. The choice of band can also have an impact on how sensitive the imaging radar is to atmospheric attenuation, the longer the wavelength, the more insensitive the system is [Campbell, 2011].

For sea ice monitoring the most commonly used band is C-band, and it has been used commercially for operational sea ice chart production since the 1990's. A range of different satellite sensors such as ERS-1/2, Envisat ASAR, Radarsat-1/2 and Sentinel-1A/B have been or are being used to produce operational ice charts. In addition to C-band, X-, and L-band are also frequently used., e.g. TerraSAR-X (X-band) and ALOS-2 (L-band). For remote sensing of sea ice, the use of different frequencies can be helpful in classifying different sea ice types as different frequencies can give additional information about the surface, see

[Lohse, 2021] and references therein.

3.6 Speckle Noise

When looking at a SAR image it often appear somewhat granulated, and this is what is referred to as speckle noise. Speckle is caused by the coherent interference of waves that is being reflected from many elementary scatters [Lee and Pottier, 2009]. A goal is often to reduce the speckle noise in images, and there are different ways to obtain this. A very popular approach to reduce speckle is called multi-looking. The multi-looking process is illuminating the scene with frequencies that vary slightly from each other. This is going to produce independent returns that in turn can be averaged in order to reduce the speckle noise. Or it is possible to perform local averaging that will smooth the image and the speckle will be reduced [Campbell, 2011].

3.7 Different Scattering Mechanisms

The interaction between electromagnetic waves from the radar and the targets on the ground can be described by different scattering mechanisms that is depending on a range of factors. These factors can include the electromagnetic properties of the target, as well as the geometry of the targets. Some of the main scattering mechanisms seen in radar remote sensing will be discussed in this section.

3.7.1 Single Bounce Scattering / Surface Scattering

When the incident radar wave is being dispersed only once, the scattering mechanism is referred to as single bounce scattering or surface scattering. It is often seen that targets/surfaces that are "producing" single bounce scattering are often somewhat flat surfaces relative to the wavelength of the incident radar wave. There are in the co-pol channels that the surface scattering will have the highest response [Cloude, 2010]. The roughness of the surface will have an impact on the backscattered signal, Figure [3.2] is illustrating how the scattering is controlled by the surface.

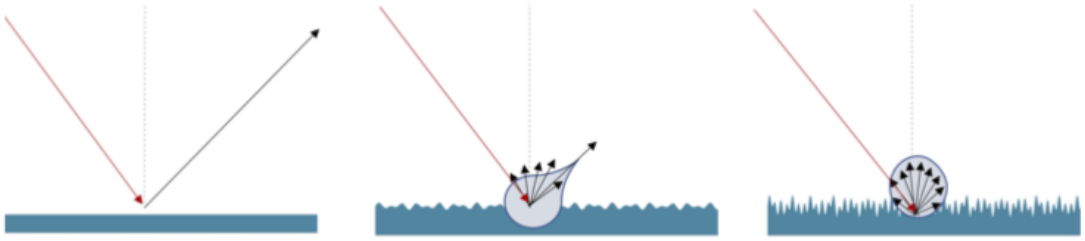

Figure 3.2: Surface Scattering for (1) smooth surface, (2) slightly rough surface, and (3) a very rough surface. (Figure used with permission of Dr. Martine Espeseth)

As can be seen in Figure [3.2] in the case of a smooth surface the backscattered signal will return without depolarization while for a very rough surface the backscattered signal is depolarized. This means that for a very rough surface the backscattered signal will generate a response in the cross-polarized channels and for a smooth surface the response will be in the co-polarized channels [Cloude, 2010]

3.7.2 Double bounce Scattering / Corner Reflection

Double bounce scattering is happening when the incident wave is bouncing twice during the interaction with the target, before it is scattered back to the receiver. In the presence of an ideal corner reflector the response will be produced only in the co-pol channels [Cloude, 2010]. Double bounce scattering can also be referred to as dihedral scattering. For sea ice double bounce scattering typically occur along the ice edges or where smooth level ice meets deformed ice.

3.7.3 Volume Scattering

Volume scattering is a scattering mechanism that can be seen within a bulk inhomogeneous material that is containing local variations in the dielectric properties [Cloude, 2010]. The dominant backscatter contribution from volume scattering may be scatters from within the material due to high penetration of the medium [Ulaby and Elachi, 1990]. In the case of sea ice where there is a presence of brine (as in first-year ice), the imaginary part of the dielectric constant will be higher, the penetration depth will be lower. For multiyear ice,

there will be a higher penetration depth, and therefore a higher amount of volume scatters [Cloude, 2010].

4

SAR Polarimetry

SAR polarimetry is an advanced radar technique utilizing the vector nature of the electromagnetic waves in order to optimize the information that is contained in the backscattered radar signal. This chapter will give an introduction to the theory behind SAR polarimetry as well as a description of its basic principles.

4.1 Polarization of Electromagnetic Waves

The electromagnetic wave that is being transmitted from a SAR system will contain both an electric and a magnetic force field. [van Zyl and Kim, 2011]. An assumption of a monochromatic plane wave is made in order to analyse the polarization of the electromagnetic wave. A monochromatic plane wave means that there is no mobile electrons on the propagation medium [Lee and Pottier, 2009]. It is possible to define the polarization of an electromagnetic wave by describing the time-space variation of the electric field plane that is oriented perpendicular to the propagation direction of the wave. A fully polarized electromagnetic wave can be represented by horizontal and vertical components [Jin and Xu, 2013].

$$\mathbf{E}(z,t) = E_{i0}\hat{e}_i e^{ik_i * r} = \hat{v}E_v + \hat{h}E_h \tag{4.1}$$

In this equation the two components E_v and E_h are representing the vertical and horizontal components of the electrical fields that in turn can be represented

as:

$$E_v = E_{0v}cos(kz - \omega t + \varphi_v) \; and E_h = E_{0h}cos(kz - \omega t + \varphi_h) \tag{4.2}$$

Where k is the wave number and ω is the angular frequency [Jin and Xu, 2013].

4.1.1 Polarization Ellipse

The wave polarization can be described by the polarization ellipse. And the polarization ellipse is describing the temporal wave trajectory with the help of the relationship between the components of $\overrightarrow{E}(z_0, t)$ [Lee and Pottier, 2009]. Equation 4.3 describes the equation for an ellipse. There are some special cases of the polarization ellipse that leads to different types of polarization [Lee and Pottier, 2009].

$$[\frac{E_x(z_o, t)}{E_{0x}}]^2 - 2\frac{E_x(z_o, t)E_y(z_0, t)}{E_{0x}E_{0y}}cos(\delta_y - \delta_x) + [\frac{E_y(z_0, t)}{E_0 y}] = sin(\delta_x - \delta_y) \tag{4.3}$$

The linear polarization is where the wave is linearly polarized when $\delta_y - \delta_x = n\pi$ (=0), and the ellipse is collapsing to a line. Linear polarization can be either vertical or horizontal. [van Zyl and Kim, 2011]. Figure 4.1 is illustrating the spatial evolution of a linear horizontal and vertical monochromatic plane wave.

Circular polarization is where the wave is circular polarized when it is rotating around the $\hat{z}$ axis in a circular way. This is occurring when $\delta = \delta_y - \delta_x = \pi/2 + n\pi$ [Lee and Pottier, 2009].

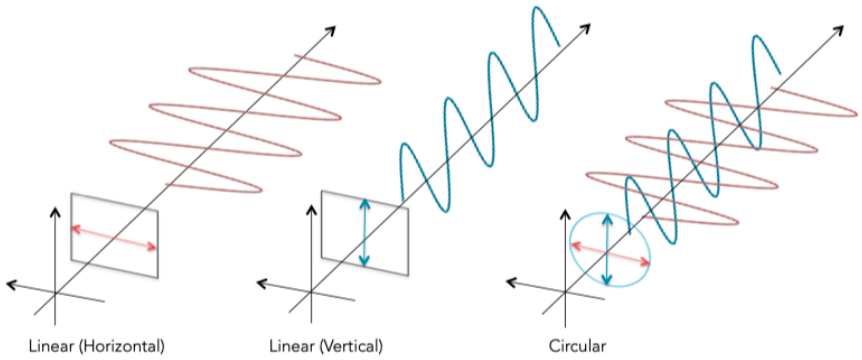

Figure 4.1: Illustration of the spatial evolution of a monocromatic plane wave (Figure used with permission of Dr. Martine Espeseth).

If the wave is polarized in any other way than described above, it is said to be elliptically polarized, and the wave will describe a trajectory that is helical around the $\hat{z}$ axis [Lee and Pottier, 2009].

4.1.2 The Jones Vector

The Jones vector can be used to describe the wave polarization of a plane monochromatic electric field by using a small amount of information [Lee and Pottier, 2009]. It is possible to represent the equations 4.1 and 4.2 as the complex Jones vector.

$$\mathbf{E} = \begin{bmatrix} E_v \\ E_h \end{bmatrix} = \begin{bmatrix} E_{0v} e^{i\varphi_v} \\ E_{0h} e^{i\varphi_h} \end{bmatrix} \tag{4.4}$$

In equation [4.4] φ_0 is representing the absolute phase. The Jones vector is used when there is coherent scattering, meaning that the fully polarized wave is incident on a target (point target or deterministic simple target) will be scattered back fully polarized [Jin and Xu, 2013].

4.2 Polarimetry in SAR Systems

A SAR system can be configured in different ways regarding the way it transmits and receives polarized energy. The system can transmit the energy horizontally and receive the backscattered energy from the target horizontally (HH case), or it can transmit horizontally and receive vertically (HV case). The system can also transmit the energy vertically and receive it vertically (VV case), or it can transmit vertically and receive horizontally (VH case) [Campbell, 2011].

SAR data can be described as single-, dual- or quad (fully)-polarimetric (pol) based on the systems ability to transmit and receive the signal. Single-pol data will only contain signal transmitted and received with one type of polarization, either HH, VV, HV or VH. Dual-pol data will contain data that is transmitted with one polarization (H or V) and received in both horizontal and vertical, HH/HV, VV/VH or HH/VV. A fully polarimetric data set will contain signal both transmitted and received horizontally and vertically, HH/HV/VV/VH. The different channels will provide different information about the target surface. For example the VV-channel is well known to be good for oil spill detection and the combination of HH/HV is commonly used for operational sea ice mapping.

Another concept of radar polarimetry is compact polarimetry (CP). In a CP system the polarization transmitted can be linear or circular, while the receivers are still linear and able to receive either vertical or horizontal polarizations

[Souyris et al., 2007]. For a fully polarimetric radar system it is possible to perform a change of polarimetric basis, meaning it is possible to simulate a right (or left) hand circular system. [Lee and Pottier, 2009] For this thesis this is a technique used in the generation of the Stokes vector, which is further described in section [4.3.2].

4.2.1 Scattering Matrix / Sinclair Matrix

As described in section 4.1.2, it is possible to represent the polarization of a plane (monochromatic) electric field with the help of the Jones vector, presented in equation 4.4. An expression of the scattering process at a specific target can therefore be expressed as in equation [4.5] [Lee and Pottier, 2009].

$$\underline{E}_S = \frac{e^{-jkr}}{r}\mathrm{S}\underline{\mathrm{E}}_\mathrm{I} = \frac{e^{-jkr}}{r}\begin{bmatrix} S_{11} & S_{12} \\ S_{21} & S_{22} \end{bmatrix}\underline{\mathrm{E}}_\mathrm{I} \tag{4.5}$$

In equation [4.5] $\underline{E}_S$ is the scattered electric field represented by the Jones-vector, $\underline{E}_I$ is the incident electric field represented by the Jones vector. The term $(\frac{e^{-jkr}}{r})$ is representing the effects of propagation, that can occur for both the phase and for the amplitude. Finally, the S-matrix is the scattering matrix or also called the Sinclair matrix. By using the Sinclair matrix it is possible to derive the complex scattering coefficients. The diagonal elements of the matrix are what is called the co-pol elements. The co-pol elements are relating the same polarizations for the incident fields and scattered fields (HH, VV). The off-diagonal elements are relating orthogonal polarization states (HV, VH) and therefore called the cross-pol elements of the scattering matrix [Lee and Pottier, 2009].

4.3 Describing Polarimetric Targets

There are multiple different ways and techniques that can be utilized to describe the fully polarimetric SAR data. The Sinclair matrix are often the foundation of these techniques, and by using the Sinclair matrix it is possible to further use techniques based upon different matrices and vectors. Examples of vectors and matrices that can be used to describe polarimetric targets is the Covariance matrix and Coherency matrix [Lee and Pottier, 2009]. It is these so-called *polarimetric target descriptors* that are used in different decomposition theories, and it is therefore important to get an understanding of the various polarimetric target descriptors.

4.3.1 Covariance and Coherency Matrices

A commonly used way to utilize all the information related to the target is to look at the covariance matrix and the coherency matrix. These matrices are used in various decomposition theories, and a very common use of the coherency matrix is the Pauli decomposition, where the diagonal elements of the coherency matrix is used to create a RGB color composite [Lee and Pottier, 2009].

The Hermitian outer product is used to find the covariance matrix described in equation [4.6] [Lee and Pottier, 2009]

$$C = \frac{1}{L}\sum_{i=1}^{L} k_l k_l^* = \begin{bmatrix} < |S_{HH}|^2 > & \sqrt{2} < S_{HH}S_{HV}^* > & < S_H HS_{VV}^* > \\ \sqrt{2} < S_{HV}S_{HH}^2 > & 2 < |S_{HV}|^2 > & \sqrt{2} < S_{HV}S_{VV}^* > \\ < S_{VV}S_{HH}^* > & \sqrt{2} < S_{VV}S_{HV}^* > & < |S_{VV}|^2 > \end{bmatrix} \tag{4.6}$$

And here k_l denotes the lexiographic target vector(hence the l notation), that can be defined as:

$$k_l = [S_{HH} \quad \sqrt{S_{HV}} \quad S_{VV}]^T \tag{4.7}$$

The coherency matrix can also be found by the Hermitian outer product, but here the Pauli target vector in equation [4.8] is being used.

$$k_p = \frac{1}{\sqrt{2}}[S_{HH} + S_{VV} \quad S_{HH} - S_{VV} \quad 2S_{HV}]^T \tag{4.8}$$

By using the Pauli target vector the coherency matrix is defined as in equation [4.9].

$$\begin{aligned} \mathrm{T} &= <\mathrm{k}_p k_p^* > \\ &= \frac{1}{2}\begin{bmatrix} < |S_{HH} + S_{VV}|^2 > & < (S_{HH} + S_{VV})(S_{HH} - S_{VV})^* > & 2 < (S_{HH} + S_{VV})S_{HV}^* > \\ < (S_{HH} - S_{VV})(S_{HH} + S_{VV})^* > & < |S_{HH} - S_{VV}|^2 > & 2 < (S_{HH} - S_{VV})S_{HV}^* > \\ 2 < S_{HV}(S_{HH} + S_{VV})^* > & 2 < S_{HV}(S_{HH} - S_{VV})^* > & 4 < |S_{HV}|^2 > \end{bmatrix} \end{aligned}$$

(4.9)

4.3.2 The Stokes Vector

When describing incoherent systems the Stokes vector is a good tool. A incoherent system will only be able to measure the power term of an incoming wave that is observable. As a consequence of this it is possible to use the Stokes vector to describe the polarization of an electromagnetic wave by using power measurements. The Stokes vector with is parameters can be gives as described in equation [4.10] [Lee and Pottier, 2009].

$$\underline{g}_{\underline{E}} = \begin{bmatrix} g_0 \\ g_1 \\ g_2 \\ g_3 \end{bmatrix} = \begin{bmatrix} E_x E_x^* + E_y E_y^* \\ E_x E_x^* - E_y E_y^* \\ E_x E_y E^* + E_y E_x^* \\ j(E_x E_y^* - E_y E_x^*) \end{bmatrix} = \begin{bmatrix} |E_|^2 + |E_y|^2 \\ |E_x|^2 - |E_y|^2 \\ 2Re(E_x E_y^*) \\ -2Im(E_x E_y^*) \end{bmatrix} \tag{4.10}$$

It is possible to utilize different outgoing wave polarizations in order to generate different Stokes vectors. Examples of different outgoing wave polarizations can be linear (either horizontal or vertical) or circular (either left handed or right handed). The Stokes vector is conveying information stored in the wave itself, and the initial state of transmittance is important when generating different Stokes vectors. In this thesis a right hand circular system will be simulated to generate the Stokes vector.

The different parameters of the Stokes vector contains different types of information; the g_0 parameter contains information about the total power density of the wave, the g_1 parameter is giving information about the power in the linear horizontally or vertically polarized components, the g_2 parameter contains information about the power in the linearly polarized components that are at tilt angles $\psi = 45°$ or $\psi = 135°$, and lastly the g_3 parameter is containing information about the power in the right-handed and the left-handed circular polarized component in the plane wave [Lee and Pottier, 2009].

It can be said that there is a presence of a polarized component in the plane wave if the value of at least one of the Stokes parameters are nonzero. And with the help of the Stokes parameters it is possible to describe the polarization of a monochromatic electromagnetic wave by being able to describe the magnitude and relative phase of the wave [Lee and Pottier, 2009]. It is also possible to establish the following relation between the Stokes parameters of a fully polarized wave [Lee and Pottier, 2009].

$$g_0^2 = g_1^2 + g_2^2 + g_3^2 \tag{4.11}$$

4.4 Decomposition Theorems

The scattering (Sinclair)- matrix [S] is a good tool when describing so-called *pure targets*, but might be insufficient when describing more complex targets. So in order to be able to fully describe the targets, different decomposition techniques are useful. Decomposition can be done in multiple ways, and is often separated into two main groups based of whether one is looking at coherent or incoherent targets.

4.4.1 Coherent Decomposition Theorems

When talking about coherent decomposition the goal is to find a way to express the scattering matrix of a simple target that is being measured by the radar. A limitation with coherent target decomposition is that the target being observed also has to be coherent [ESA,].

The Pauli Decomposition

The Pauli decomposition is using the measured scattering matrix and a so-called Pauli basis in order to express the scattering matrix as a complex sum of the different Pauli matrices [Lee and Pottier, 2009].

$$\mathbf{S} = \begin{bmatrix} S_{HH} & S_{HV} \\ S_{VH} & S_{VV} \end{bmatrix} = \frac{a}{\sqrt{2}} \begin{bmatrix} 1 & 0 \\ 0 & 1 \end{bmatrix} + \frac{b}{\sqrt{2}} \begin{bmatrix} 1 & 0 \\ 0 & -1 \end{bmatrix} + \frac{c}{\sqrt{2}} \begin{bmatrix} 0 & 1 \\ 1 & 0 \end{bmatrix} + \frac{d}{\sqrt{2}} \begin{bmatrix} 0 & -j \\ j & 0 \end{bmatrix} \tag{4.12}$$

Each of the basis matrices are here associated with an elementary scattering mechanism. The parameters a,b,c and d are all complex values and can be defined as:

$$a = \frac{S_{HH} + S_{VV}}{\sqrt{2}} \quad b = c\frac{S_{HH} - S_{VV}}{\sqrt{2}} \quad c = \frac{S_{HV} + S_{VH}}{\sqrt{2}} \quad d = \frac{S_{HV} - S_{VH}}{\sqrt{2}} \tag{4.13}$$

The Pauli decomposition can be applied to deterministic targets, and it is possible to look at the result as a coherent composition of different scattering.

4.4.2 Incoherent Decomposition Theorems

As mentioned in the introduction to decomposition theorems [section 4.4] the Sinclair matrix is a good tool when one is describing pure/coherent targets, but for incoherent targets this technique is not sufficient. It is therefore necessary to have other decomposition theorems so it can be possible to describe and/or analyse the scatters. When the scatters are incoherent, speckle noise will be

present, and when this noise is being reduced by multi-looking the polarimetric representation has to be of second order. The way to describe these scatters are then by the multi-looked covariance matrix and/or by the multi-looked coherency matrix that is described in section 4.3.1. Different decomposition techniques can be preformed on either of these two matrices [ESA,].

Eigenvalue-Eigenvector Based Decomposition

The theory that is based on eigenvalue-eigenvector decomposition is using the coherency matrix, and is finding the eigenvalues and eigenvectors from it. The decomposition can be described as in equation [4.14] [ESA,] An eigenvector decomposition will provide a description of the scatterer that is basis invariant [Lee and Pottier, 2009].

$$< T_3 >= U_3 \Sigma_3 U_3^{-1} \tag{4.14}$$

Where Σ_3 is the diagonal matrix that is containing the eigenvalues of $< T_3 >$. The eigenvectors are contained in the unitary matrix, U_3 The eigen decomposition can in turn be used to derive different second order polarimetric parameters that can be used to simplify the analysis of the physical information that is being found by the eigen decomposition. An example of a very popular eigen decomposition theory are the H/A/$\overline{\alpha}$ decomposition that is described in section [4.4.2][Lee and Pottier, 2009].

H/A/$\overline{\alpha}$ Decomposition Theorem

As mentioned the H/A/$\overline{\alpha}$ decomposition is an eigenvalue-eigenvector based decomposition theorem that is based on the assumption that there will always be an "average" dominant scattering mechanism. The theory works towards finding the parameters for the average component [Lee and Pottier, 2009]. The parameters included in this decomposition theorem will be presented in the following sections

Entropy, H The entropy parameter can be used to describe the statistical disorder of the different scatter types in the data. The calculation of the parameter is based on the pseudo-probabilities that is defined in equation [4.15] [Lee and Pottier, 2009].

$$P_i = \frac{\lambda_i}{\sum_{k=1}^{3} \lambda_k} \quad with: \quad \sum_{K=1}^{3} P_k = 1 \tag{4.15}$$

Where λ_i are the eigenvalues of the coherency matrix. Using this it is possible to define the entropy parameter.

$$H = -\sum_{k_1}^{N} P_k log_n(P_k) \tag{4.16}$$

P_i is the pseudo-probabilities calculated by equation [4.15], N is the logarithm basis and have to be equal to the polarimetric dimension (3 for the monostatic case or 4 for the bistatic case). Since the eigenvalues are considered to be rotational invariant, the entropy is a roll-invatiant parameter [Lee and Pottier, 2009].

Low entropy scatters can be expected over the ocean, while high entropy scatters are expected over parkland regions and over deformed sea ice areas and multi-year ice. High entropy indicated that there is more depolarization and there will be a presence of different scattering mechanisms. Entropy is a parameter that can be used to give information related to the roughness of the surface, which can be utilized in sea ice studies to say something about the roughness of the ice [Lee and Pottier, 2009].

Anisotropy, A The eigenvalues of the coherency matrix are in sequential order, and this fact is being utilized by the anisotropy parameter which is defined in equation [4.17] [Lee and Pottier, 2009].

$$A = \frac{\lambda_2 - \lambda_3}{\lambda_2 + \lambda_3} \tag{4.17}$$

The anisotropy is also a roll-invariant parameter, and it is measuring the relative importance of the third and second eigenvalues. It can therefore be used as a compliment to the entropy parameter. For higher entropy values(H>0.7) the parameters will to a lesser degree be affected by noise, and it is therefore in these cases the anisotropy is best used [Lee and Pottier, 2009].

Mean Alpha angle, $\overline{\alpha}$ The mean alpha angle is a polarimetric parameter that can be used to identify scattering mechanisms. The alpha angle, α is defined in equation [4.18].

$$\alpha = cos^{-1}(|e_i|), i = 1, 2, 3 \tag{4.18}$$

Where e_i is the eigenvector of the coherency matrix. The parameter is best represented by looking at the mean, and do to this the pseudo-probabilities defined in equation [4.15] are used.

$$\overline{\alpha} = \sum_{k=1}^{3} P_k \alpha_k \tag{4.19}$$

The $\overline{\alpha}$ parameter defined in equation [4.19] will register a change in the surface scattering, and based on the size of the angle it is possible to determine type of scattering mechanism. For very high values of $\overline{\alpha}$ there is a presence of dihedral scatter, which often can occur when there is a metallic surface. With a decrease in the value there is a higher presence of double bounce scattering, and even lower values of $\overline{\alpha}$ can represent dipole or single bounce scattering. For the lowest values of $\overline{\alpha}$ there is a presence of surface scattering [Lee and Pottier, 2009].

The H/A/$\overline{\alpha}$ decomposition theory can be used to say something about the scattering mechanisms present in an image, and in this study this is used to asses the data before the analysis. Results of H/A/$\overline{\alpha}$ decomposition can be seen in section [6.5].

5

Data and Study Area

5.1 Description of the Data Used

The data used in this thesis are fully polarimetric Radarsat-2 C-band (5.405 GHz) data. The images are collected during the winter months and with various incident angles, though consists of two data sets each of them covering the same sea ice within a short time period (Less than eight hours) though with different incidence angles. An overview of the data used is presented in table [5.1]. The images have a range and azimuth resolution of 5.2 m x 7.6 m.

Table 5.1: Overview of data used in the study, (https://arvenetternansen.com)

	Date	Time (UTC)	Incidence angle
Data Set 1	02.12.2019	12:43	20
	02.12.2019	06:03	35
	02.12.2019	14:23	40
Data Set 2	04.12.2019	13:25	28
	04.12.2019	15:05	47

5.2 Study Area

The images were collected during a in-situ data campaign as a part of the Nansen Legacy program north of Svalbard in 2019. For more information about

the program see https://arvenetternansen.com. At the time of the image acquisitions the air temperature was -14^{o}C and the wind speed 7 m/s. The scene locations are presented in Figure [5.1a], with a more detailed image on how the scenes in the different data sets are located relevant to each other in Figure [5.1b].

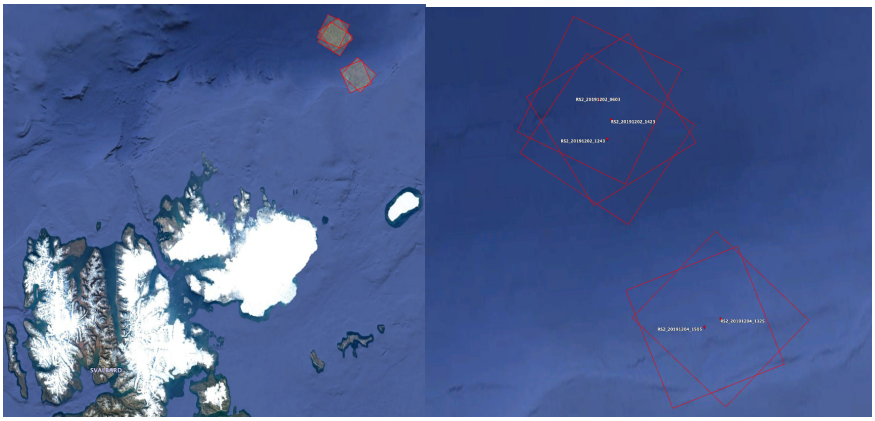

(a) **(b)**

Figure 5.1: Location of the SAR images, where a) shows the larger study area including Svalbard and b) shows the zoomed in version.

6 Method

The method consists of three separate steps; the segmentation of the images, the subsequent classification and the extraction of the four different polarimetric parameters. In this chapter the polarimetric parameters investigated in this study are presented, the segmentation and classification process explained as well as an evaluation of the data itself considering noise and scattering mechanisms.

6.1 Calibration

As a first step all Radarsat-2 scenes are calibrated before any analysis is performed. Radiometric calibration is a pre-prosessing step, and for the data in this thesis the radiometric calibration has been performed using SNAP (Esa software). Moreover is reciprocity of the data assumed, and the cross-pol coefficients are represented as described in equation [6.1].

$$S_x = \frac{1}{\sqrt{2}}(S_{hv} + S_{vh}) \tag{6.1}$$

6.2 Polarimetric Parameters

In this thesis four polarimetric parameters have been selected to be investigated, the co-polarization ratio, the M-parameter, the degree of polarization and the polarimetric coherence. The specifics for the respective parameters as well as some interpretations are described below. When the parameters are extracted they are also multi-looked to 9x9 pixels.

6.2.1 Co-Polarization Ratio

The ratio between the co-polarized elements of the covariance matrix defined as:

$$\gamma_{VV/HH} = \frac{< S_{VV} S_{VV}^* >}{< S_{HH} S_{HH}^* >} \tag{6.2}$$

By looking at the ratios between the channels it is possible to utilize the fully polarimetric data further, as the power difference (in dB) between specific polarizations are quantified giving the characteristics if the fully polarized signature [Drinkwater et al., 1992]. As shown in, e.g., [Gill et al., 2013] the thin ice thickness has a correlation with a decrease in the co-polarization ratio. The co-polarization ratio is dependent on the dielectric properties of the surface [Moen, 2015]. Using this dependency and the fact that dielectric properties between sea ice and water are different (3.4 for ice and 80 for water [Martinez and Byrnes, 2002]), the co-polarization ratio can be used to discriminate between sea ice and open water. According to a study performed by [Gill et al., 2013] the co-polarization is negligible affected by a change in the incidence angle.

6.2.2 M-Parameter

The M-parameter is also a parameter presented in [Cloude, 2010], and as well as the polarimetric coherence is it derived from the coherency matrix:

$$M(\theta, \epsilon_r) = \frac{T_{22} + T_{33}}{T_{11}} = \frac{< |S_{HH} - S_{VV}|^2 > +4 < |S_{HV}|^2 >}{< |S_{HH} + S_{VV}|^2 >} \tag{6.3}$$

The M-parameter is not affected by the surface roughness, and can not be used to assess the depolarization level of the radar signal. It is a material indicator,

and will be affected by changes in the dielectric constant. An increase in the dielectric constant should lead to an increase in the M-parameter values. Changes in incidence angle will also have an impact on the M-parameter [Cloude, 2010].

6.2.3 Degree of Polarization

Degree of Polarization (DoP) is a parameter that is based on the Stokes vector. Here we assume a right hand circular system. As described in section [4.3.2], the Stokes vector has been derived by using compact polarimetry, and DoP is defined as in equation [6.4].

$$DoP = \frac{\sqrt{q_1^2 + q_2^2 + q_3^2}}{q_0} \tag{6.4}$$

The DoP can be looked at as the ratio of power densities of the polarized part of the wave, and the total wave [Mott, 2006]. DoP will result in a value between 0 and 1, where DoP = 0 when the wave is totally depolarized and DoP = 1 when the wave is fully polarized [Lee and Pottier, 2009]. This parameter can be used to say something about the roughness of the surface, as the rougher a surface is, the more depolarized the returning wave will be.

6.2.4 Polarimetric Coherence

Polarimetric Coherence (R) is a parameter presented in [Cloude, 2010], and can be derived using the coherency matrix as follows:

$$R(\delta) = \frac{T_{22} - T_{33}}{T_{22} + T_{33}} = \frac{< |S_{HH} - S_{VV}|^2 > -4 < |S_{HV}|^2 >}{< |S_{HH} - S_{VV}|^2 > +4 < |S_{HV}|^2 >} \tag{6.5}$$

R is related to the surface roughness, and indicates the level of depolarization of the signal. If R = 0, the returning signal has been depolarized by the surface, and the surface can be considered very rough. On the other hand, if R = 1 the level of depolarization is low, and the surface can be considered to be very smooth. The R parameter should not be affected by a difference in incidence angle, and is also not sensitive to changes on the surface that will affect the dielectric constant of the ice, like salinity and moisture content of the ice [Cloude, 2010]. Meaning that the parameter could possibly be used also during the early and advanced melt season time period.

6.3 Segmentation and Classification

The calibrated images were segmented using the method outlined in [Doulgeris, 2013] and [Doulgeris and Eltoft, 2010], and the different segments were analysed and classified into sea ice types by sea ice experts. The classes used in this study are:

- Class 1 - Bright Young Ice (high backscatter)
- Class 2 - Dark Young Ice (low backscatter)
- Class 3 - Smooth Ice
- Class 4 - Deformed Ice
- Class 5 - Open Water (Only relevant for data set 2)

A median filter was applied to the segmented areas to remove outlying areas with single or low number of pixels. The median filter works by sliding a window of a given size over the image to be filtered, and replacing each pixel value with the median pixel value of the local neighbourhood/window [Jain et al., 1995]. In this case a [20x20] sized window has been used. An example of unfiltered and corresponding filtered images can be seen in Figures [6.1 and 6.2] respectively. The classified segments were used to produce binary masks to extract the polarimetric feature values corresponding to the different sea ice types.

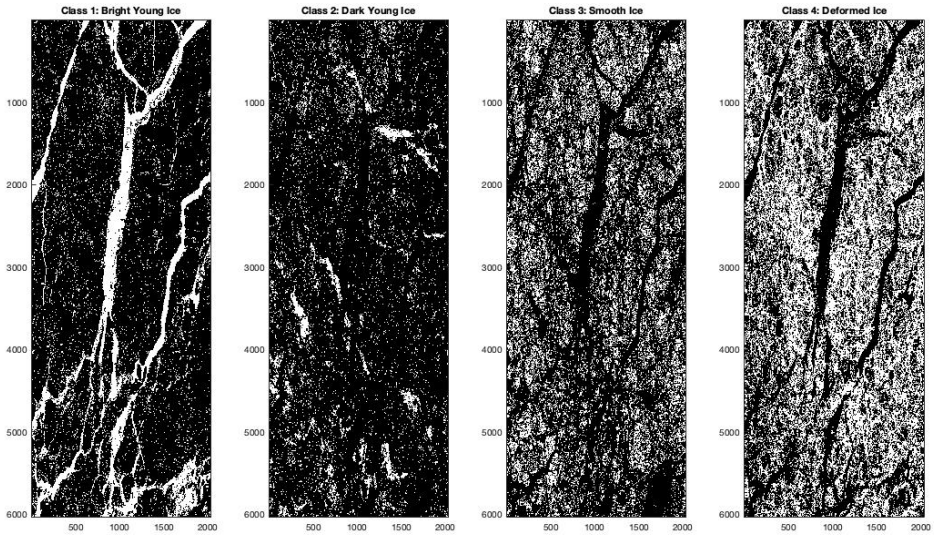

Figure 6.1: Example of unfiltered masks for segmented Radarsat-2 image from 02.12.2019 - 12:43UTC. White pixels corresponds to the different sea ice types, where bright young ice is shown to the left, dark young ice second, smooth ice in the third image and deformed sea ice to the right.

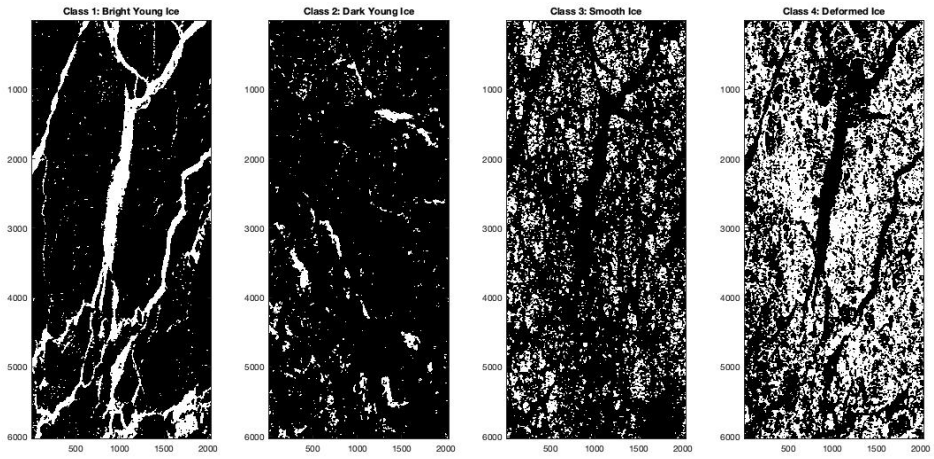

Figure 6.2: Example of filtered masks for segmented Radarsat-2 image from 02.12.2019 - 12:43UTC. White pixels corresponds to the different sea ice types, where bright young ice is shown to the left, dark young ice second, smooth ice in the third image and deformed sea ice to the right.

6.4 Noise Analysis

The signal-to-noise ratio (SNR) is something to consider when analysing the results. If the data is close to or below the noise equivalent sigma zero (NESZ) values, also commonly referred to as the noise floor, it can have an impact on the parameters extracted in this study. In order to determine if the data used in this study is affected by noise a noise study is performed by looking at the mean value of the HV-channel compared to the min-max values of the NESZ profile of the data. The mean of the HV-channel is looked at separately for the different classes. The noise profile is extracted from the product meta data, and the results for the different data sets can be seen in Figure [6.3] and [6.4].

In [Espeseth et al., 2020] they found that the SNR should ideally be 10 dB for the polarimetric features to not be affected by the noise levels. Out of the parameters used in this study, [Espeseth et al., 2020] investigated the DoP and co-polarization ratio and found that an SNR of 10 dB was needed for the DoP parameter but that the co-polarization ratio was less sensitive though and SNR of 3 dB was preferable. As can be seen from the noise analysis some of the classes has HV-values that are located close to the noise floor, which can have an impact on the extracted parameters. As can be seen in Figures [6.3] and [6.4] only the deformed ice class (Class 4) full-fills the 10 dB criteria for all images, and the bright young ice (Class 1) for two of the images, the 12:43 UTC image in data set 1 and 06:03 UTC image in data set 2. It is especially *Class 2 - Dark Young Ice* and *Open Water Class (Class 3)* that are impacted by a low SNR. Care must therefore be taken when interpreting the results from the classes with a low SNR, in particular for the polarimetric parameters that includes the HV-channel.

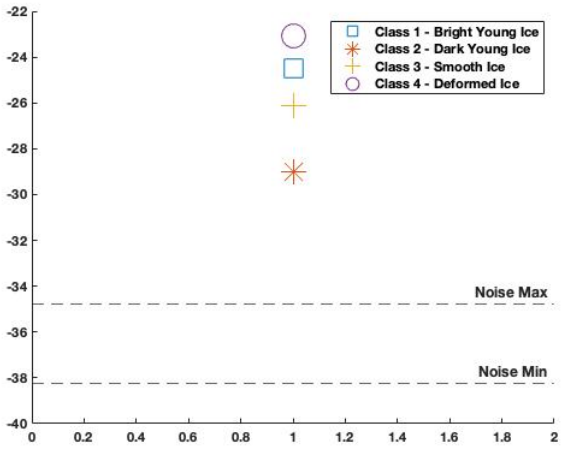

(a) 12:43

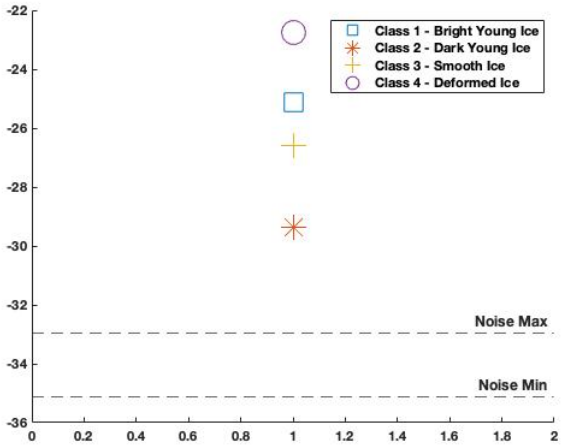

(b) 06:03

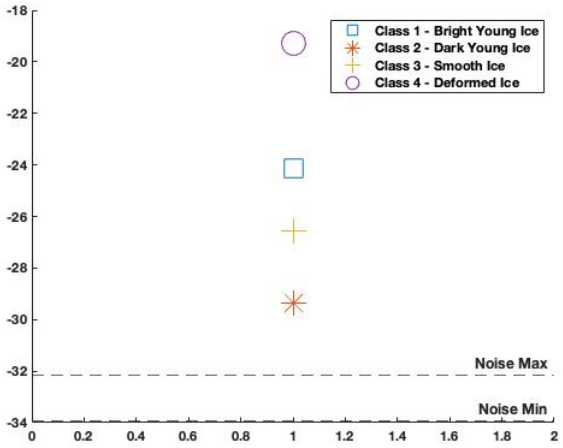

(c) 14:23

Figure 6.3: Noise analysis of data set 1

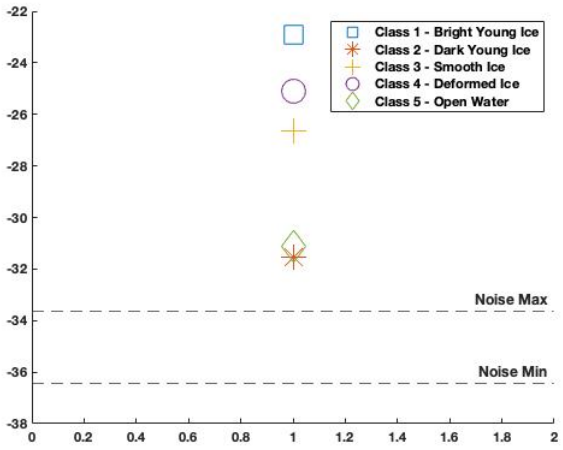

(a) 06:03

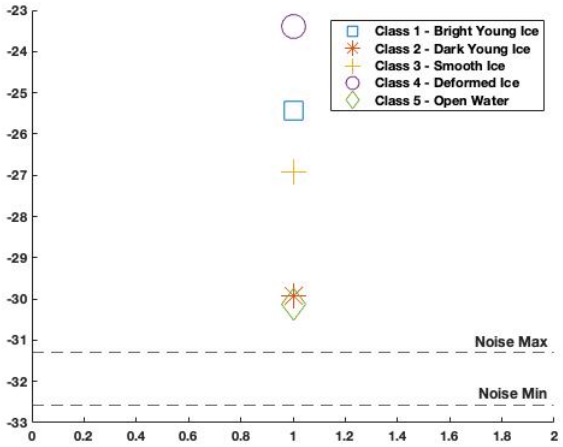

(b) 12:43

Figure 6.4: Noise analysis of data set 2

6.5 H / A / $\overline{\alpha}$ Decomposition

The eigenvalue-based H / A / $\overline{\alpha}$ decomposition is often used to provide information related to the different scattering mechanisms present in each scene, which again can provide information to the relevant classes. The theory behind this decomposition and the definition of its parameters is described in section [4.4.2]. The RGB-image results for the images used within this study can be seen in Figure [6.5] and [6.6].

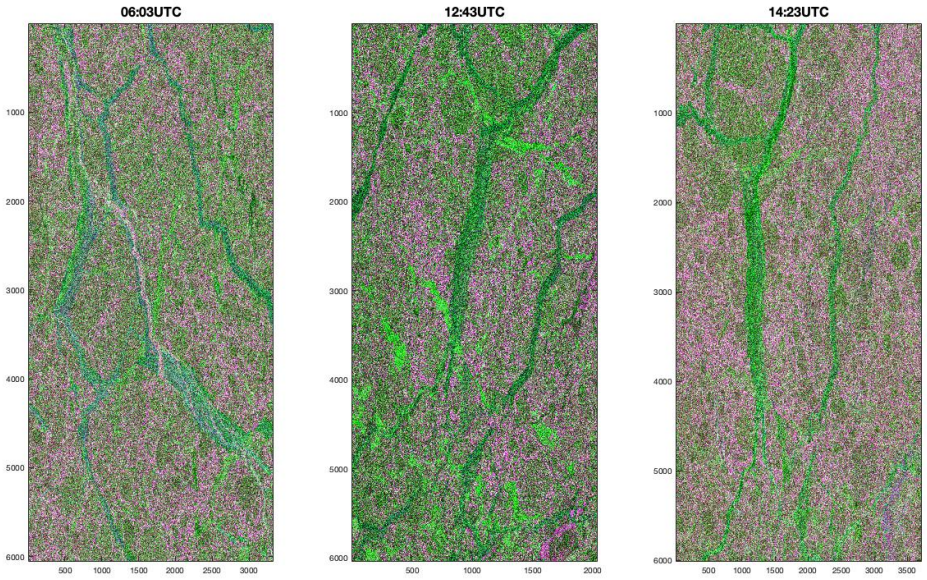

Figure 6.5: H / A / $\overline{\alpha}$ Decomposition for data set 1. Here Entropy(H) = R, Anisotropy(A) = G and $\overline{\alpha}$ = B

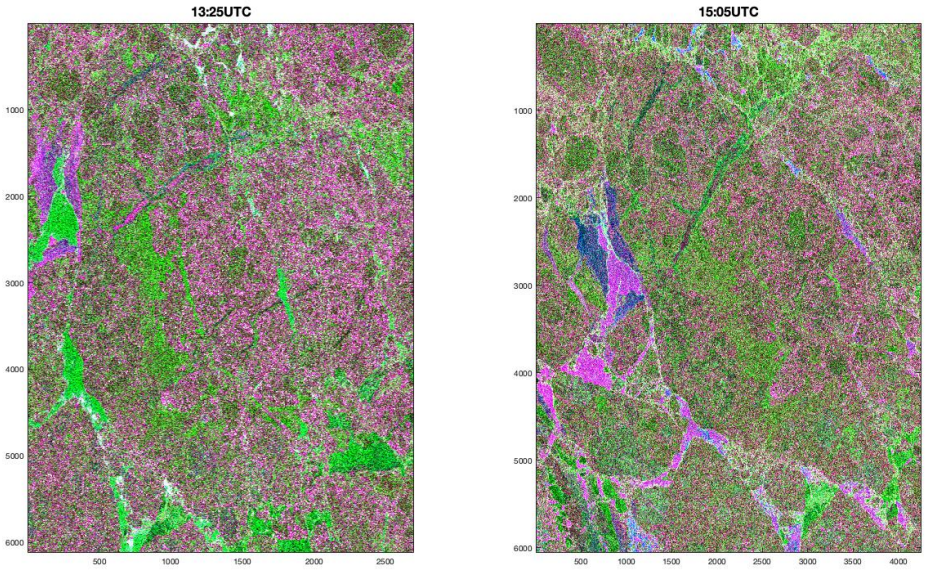

Figure 6.6: H / A / $\overline{\alpha}$ Decomposition for data set 2. Here Entropy(H) = R, Anisotropy(A) = G and $\overline{\alpha}$ = B

In data set 1 (Figure [6.5]) the areas with high entropy values (the pink/purple areas in the image) looks to be located in the areas where it is expected to find the deformed ice types. This relates well back to the theory in section [4.4.2] stating that areas with high entropy values indicates more depolarization which again can be related to the roughness of the surface. The leads are also clearly visible in the RGB images, with blue and green color, meaning the scattering mechanisms in these areas are represented by dipole or single bounce scattering, and some areas also with surface scattering. Low values of $\overline{\alpha}$ corresponds with this observation. In the case of low incidence angle seen in the middle image of Figure [6.5] (and also in the left image of Figure [6.6]), the leads and areas with thinner ice types are presented as a brighter green. This shows that also the H/A/$\overline{\alpha}$ Decomposition are sensitive to changes in incidence angle.

For data set 2 (Figure [6.6]) there looks to be variations between the images, with high entropy values over the areas with open water for the image with high incidence angle (image to the right in Figure [6.6]) and low values in the case with low incidence angle. Looking at the rest of the image, there still looks to be higher entropy values in areas where deformed ice is expected.

7

Results and Discussion

In this chapter the results will be presented and discussed, where each parameter will be presented and discussed individually followed by a joint summary and conclusion.

7.1 Co-Polarization Ratio

The co-polarization estimates (in dB) for data set 1 are shown in Figures [7.1a, 7.2a, 7.3a] and for data set 2 in Figures [7.4a and 7.5a]]. In addition are histograms for each image representing the individual classes presented in Figures [7.1b, 7.2b, 7.3b] for data set 1 and in Figures [7.4b and 7.5b] for data set 2.

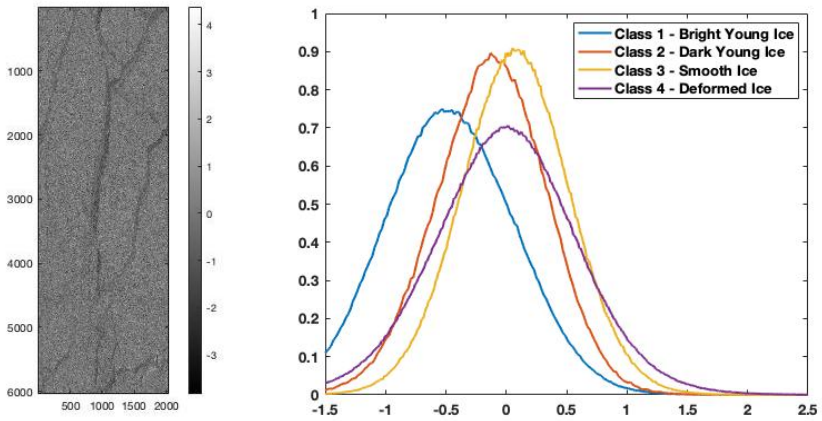

(a) **(b)**

Figure 7.1: Images taken at 12:43 UTC on 02.12.2019, with incidence angle 20°, where a) is the grey level image of co-polarization ratio, and b) histograms of co-polarization ratio separated by classes.

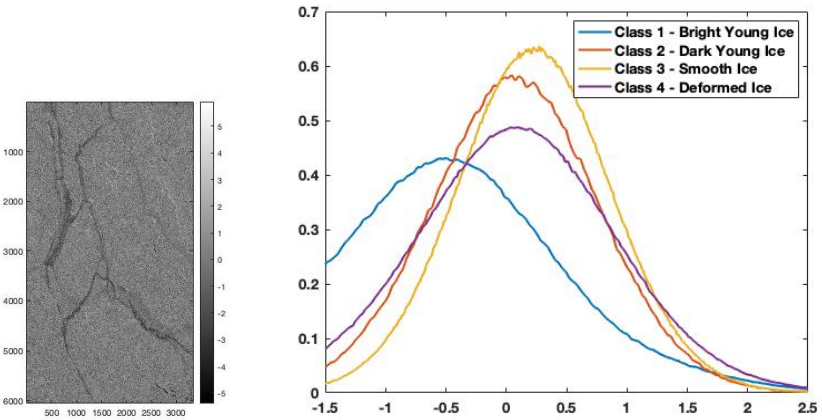

(a) **(b)**

Figure 7.2: Images taken at 06:03 UTC on 02.12.2019, with incidence angle 35°, where a) is the grey level image of co-polarization ratio, and b) histograms of co-polarization ratio separated by classes.

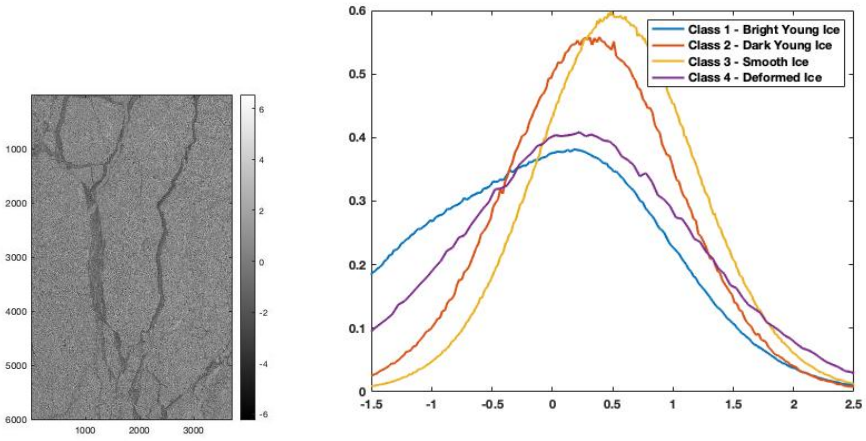

(a) **(b)**

Figure 7.3: Images taken at 14:23 UTC on 02.12.2019, with incidence angle 40^o, where a) is the grey level image of co-polarization ratio, and b) histograms of co-polarization ratio separated by classes.

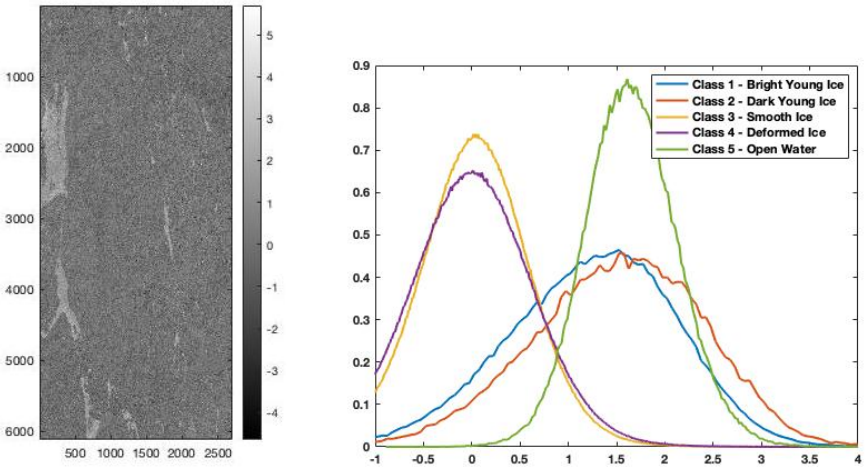

(a) **(b)**

Figure 7.4: Images taken at 13:25 UTC on 04.12.2019, with incidence angle 28^o, where a) is the grey level image of co-polarization ratio, and b) histograms of co-polarization ratio separated by classes.

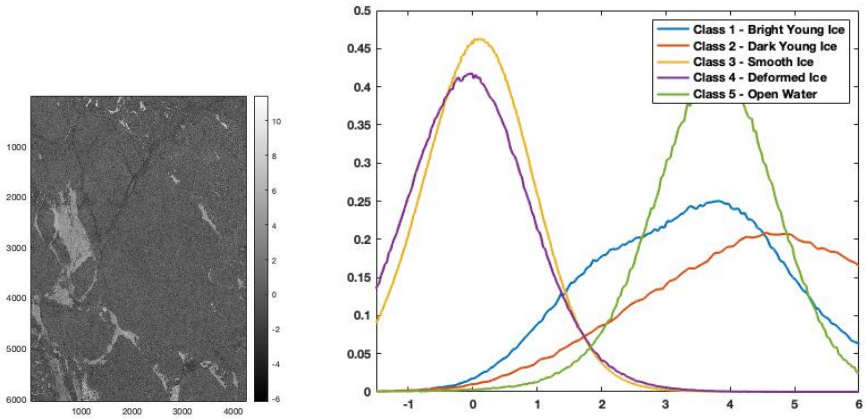

(a) **(b)**

Figure 7.5: Images taken at 15:05 UTC on 04.12.2019, with incidence angle 47^o, where a) is the grey level image of co-polarization ratio, and b) histograms of co-polarization ratio separated by classes.

It can be observed in Figures [7.1a, 7.2a and 7.3a] the areas with thinner sea ice types have negative co-polarization ratio values. By instead using the absolute value for the co-polarization ratio, as shown in Figure [7.6], it can be seen that the magnitude of the values are in line with those observed by, e.g., [Johansson et al., 2018]. The reason for this negative "shift" in the parameter is presently unknown, and are beyond the scope of this thesis but could be explored in future work.

Observing the co-polarization estimates it can be noted that the co-polarization ratio have higher absolute values in areas with thinner ice types (leads) in both data sets. The smooth and deformed sea ice classes have similar mean values and distributions. From the histograms for data set 1 we can observe limited separability between the different classes, although the bright (high backscatter) young ice is somewhat separated from the rest, having lower values. Data set 2 includes open water, and observing the histogram result presented in Figures [7.4b and 7.5b] there is a clear separation of the open water class. There is also a separation between the thinner ice types (bright young ice class and dark young ice class) from the thicker ice types (smooth ice class and deformed ice class), although it is difficult to separate these from each other. This is consistent with a study performed by Gill et. al. [Gill et al., 2013], which states that the co-polarization ratio is a good parameter to separate open water from sea ice classes. Looking at the impact of change in the incidence angle, data set 1 looks to have better separability for the lower incidence angle, seen in Figure [7.1b] than for the higher incidence angle case in Figure [7.3b]. In data set 2 the separability between open water and the thinner ice types

from the other classes looks to be good for both cases.

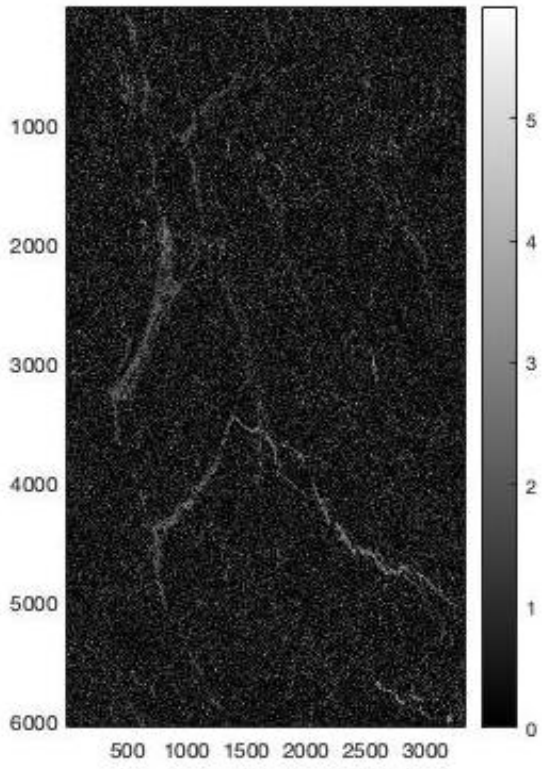

Figure 7.6: Grey level image of co-polarization parameter for image 06:03UTC. Here is the absolute value of the parameter presented, showing higher values for the thinner ice types.

For the result in data set 1 it is possible to observe the effect of varying incidence angles, but for data set 2 there is still good separability even with changing incidence angle. It can be seen that the mean values are higher for the case with higher incidence angle (with dB values around 4 for the high incidence case, and around 1.5 for the lower incidence angle), this observation corresponds with what was found in Johansson et al. [Johansson et al., 2018], which displays similar values of to co-polarization ratio over open water for similar high and low incidence angles. Also Geldsetzer in [Geldsetzer and Yackel, 2009] studied the co-polarization ratio and found a threshold of $\gamma_{VV/HH} = 2.8$ dB that can be used for separation between thin ice and open water. It should be noted that this threshold holds up for higher incidence angles, as lower incidence angles will give lower values of the co-polarization ratio for open water.

Noise will have an impact on this parameter, but as it is not dependent on

information of the HV-channel the impact will be less than on some of the other parameters investigated here.

7.2 M-Parameter

The grey level images of the M-parameter is presented in Figures [7.8a, 7.7a, 7.9a, 7.10a and 7.11a]. Figures [7.7b, 7.8b and 7.9b] is representing the histogram result of the M-parameter in data set 1 and Figures [7.10b and 7.11b] is the histogram result for data set 2.

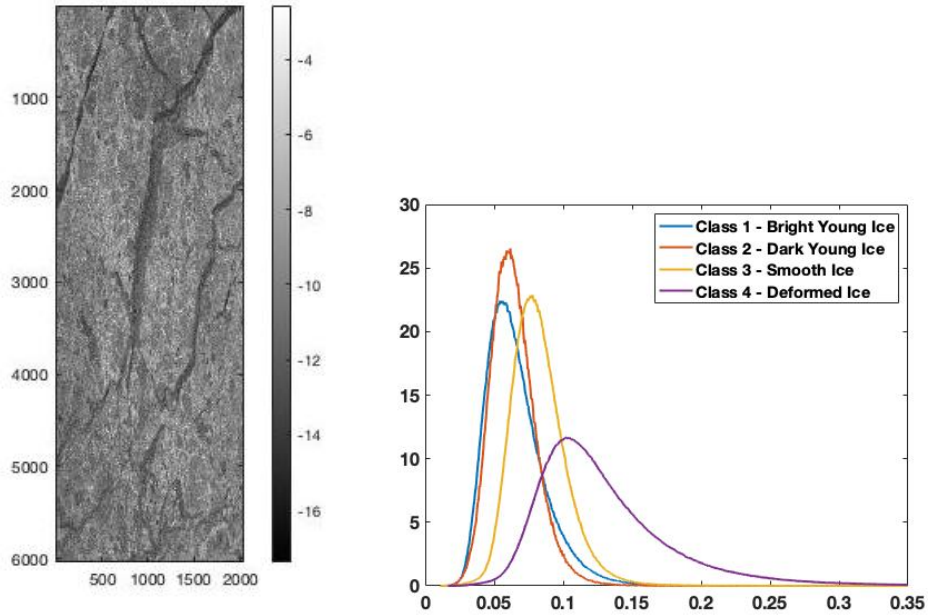

(a) **(b)**

Figure 7.7: Images taken at 12:43 UTC on 02.12.2019, with incidence angle 20^o, where a) is the grey level image of M-parameter, and b) histograms of M-parameter separated by classes.

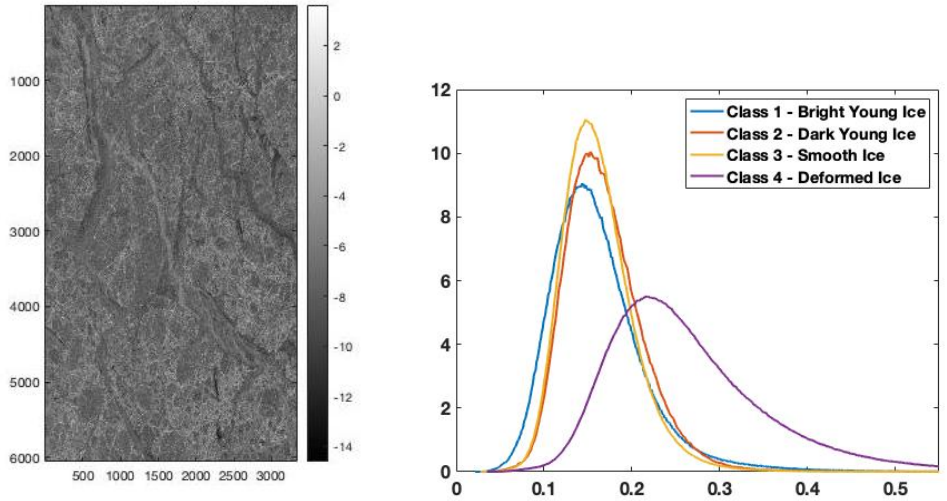

(a) **(b)**

Figure 7.8: Images taken at 06:03 UTC on 02.12.2019, with incidence angle 35^o, where a) is the grey level image of M-parameter, and b) histograms of M-parameter separated by classes.

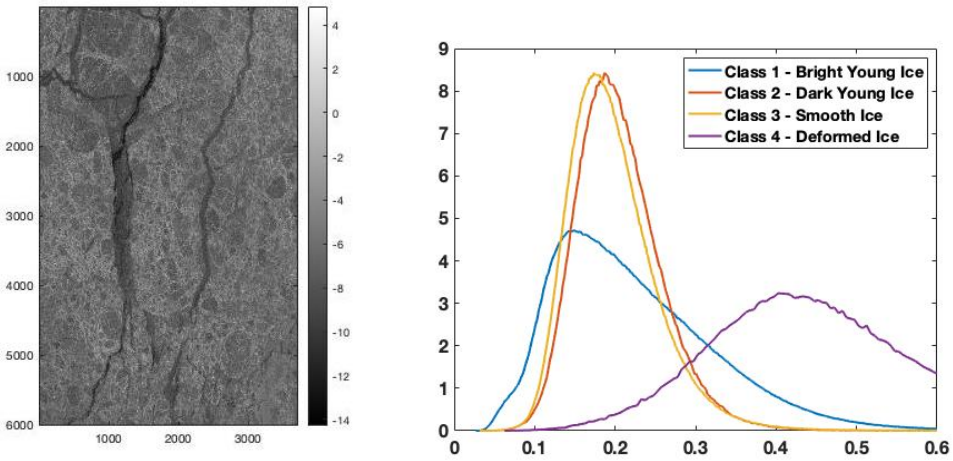

(a) **(b)**

Figure 7.9: Images taken at 14:23 UTC on 02.12.2019, with incidence angle 40^o, where a) is the grey level image of M-parameter, and b) histograms of M-parameter separated by classes.

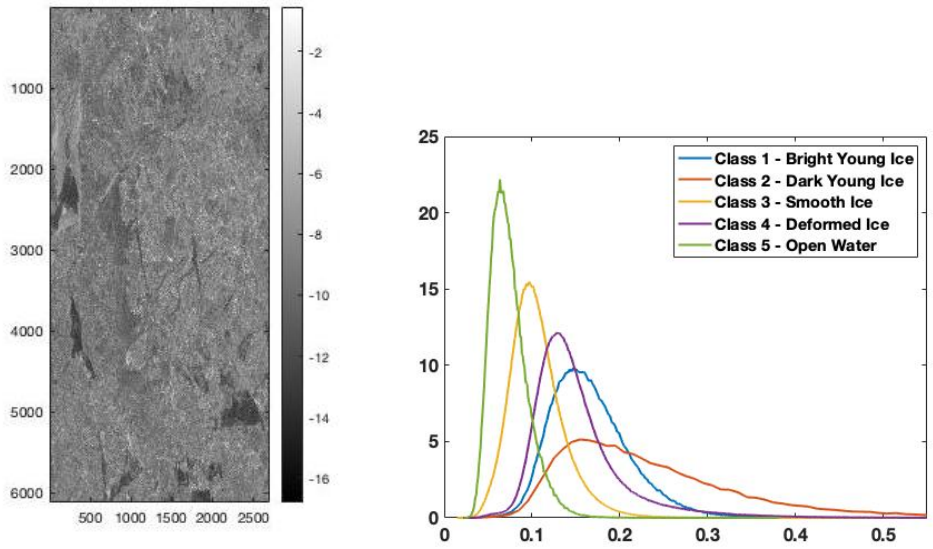

(a) **(b)**

Figure 7.10: Images taken at 13:25 UTC on 04.12.2019, with incidence angle 28^o, where a) is the grey level image of M-parameter, and b) histograms of M-parameter separated by classes.

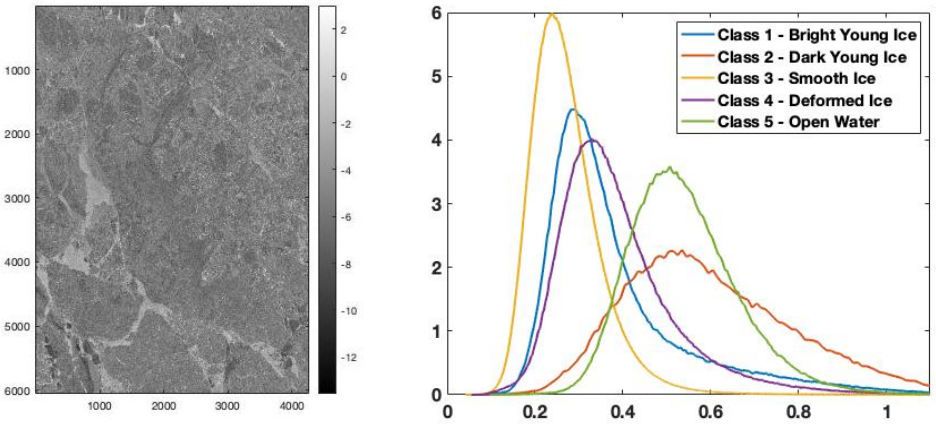

(a) **(b)**

Figure 7.11: Images taken at 15:05 UTC on 04.12.2019, with incidence angle 47^o, where a) is the grey level image of M-parameter, and b) histograms of M-parameter separated by classes.

Higher values of this parameter are expected in areas with higher dielectric constant, and according to [Brekke et al., 2014] the dielectric constant is expected to be higher for thinner ice, and decrease as the ice thickens. During

the first 5 mm of growth there is a rapid decrease in the dielectric constant, from 80 to 11. As the ice continues to thicken the dielectric constant slowly continues to decrease [Brekke et al., 2014]. For data set 1 the grey level images seem to show that the areas with thinner ice have lowest values and the same can be observed for the low incidence angle (Figure [7.10a]) image in data set 2, while the higher incidence angle case seen in Figure [7.11a] have high values in these same areas. The reason this low values for the M-parameter is unknown, and could be an interesting study for future work. Though it should be noted that as the M-parameter is derived using both the co-polarised and cross-polarised channels and the SNR for dark young ice as well as the open water areas in the data sets is not ideal, which might have an effect on the results for this data set. The result for data set 2 (Figures [7.10b and 7.11b]) shows that the open water class displays both high and low values depending on the incidence angle.

In the histograms shown in Figures [7.7b, 7.8b, 7.9b, 7.10b and 7.11b] it is possible to observe that the parameter looks to be useful in separating the deformed ice class from the other classes. Cloude [Cloude, 2010] describes the M-parameter to not be affected on the roughness on the surface, though the results in Figures [7.7b, 7.8b and 7.9b] show that the deformed ice class has the best separability from the other classes. A reason for this might be that thin ice and thicker deformed ice will have different dielectric constants, which is affecting the parameter. According to Cloude [Cloude, 2010] the M-parameter will be affected by a change in the incidence angle. Figure [7.12] shows the M-values for both the deformed ice and smooth ice plotted against the incidence angle, for data set 1. Here we can observed an incidence angle dependency, and more so for the deformed ice class that increases with increased incidence angle. The standard deviation is also observed to increase with increasing incidence angle for both the deformed and the smooth sea ice types. Also the separation between deformed ice and smooth ice seem to increase with increasing incidence angle. The fitted lines seen in Figure [7.12] is created as a visual effect connecting the points using *polyfit* in Matlab.

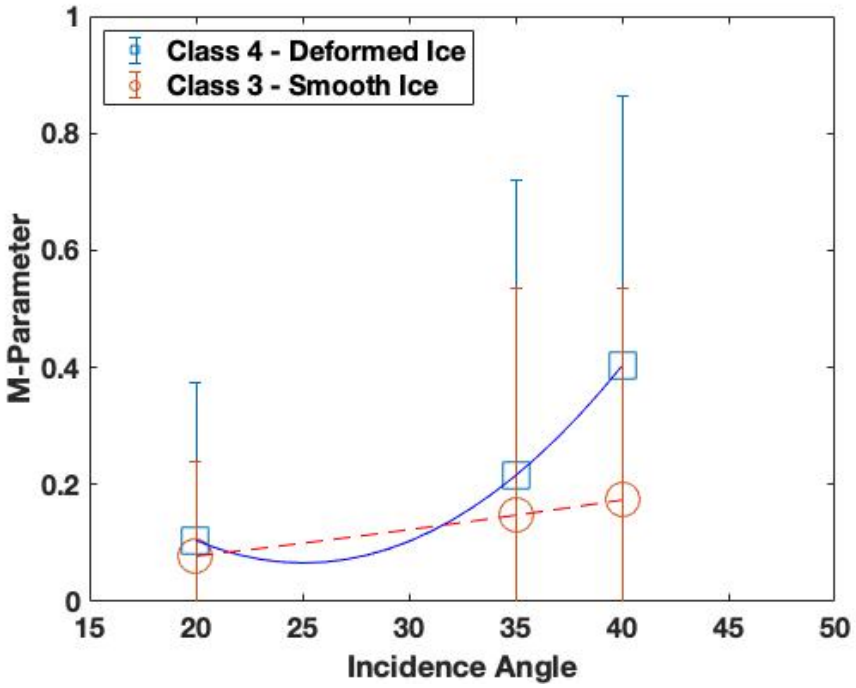

Figure 7.12: Mean and standard deviation of the M-parameter for data set 1 plotted against incidence angle for deformed ice and smooth ice classes.

In summary the M-parameter, when the data have a good SNR, looks to separate well between deformed ice and other sea ice types, but changes in incidence angle will have an effect on this parameter. The SNR for especially dark young ice and open water in data set 2 and the dark young ice in data set 1 looks to have SNR values close to the noise floor, and will likely have an impact on the results for data set 2.

7.3 Degree of Polarization

The grey level images for the Degree of Polarization parameter for data set 1 are shown in Figures [7.13, 7.14a and 7.15a] and the results for data set 2 in Figures [7.16a and 7.17a]. Figures [7.13b, 7.14b and 7.15b] and [7.16b and 7.17b] presents the histograms for each image representing the individual classes for data set 1 and 2 respectively.

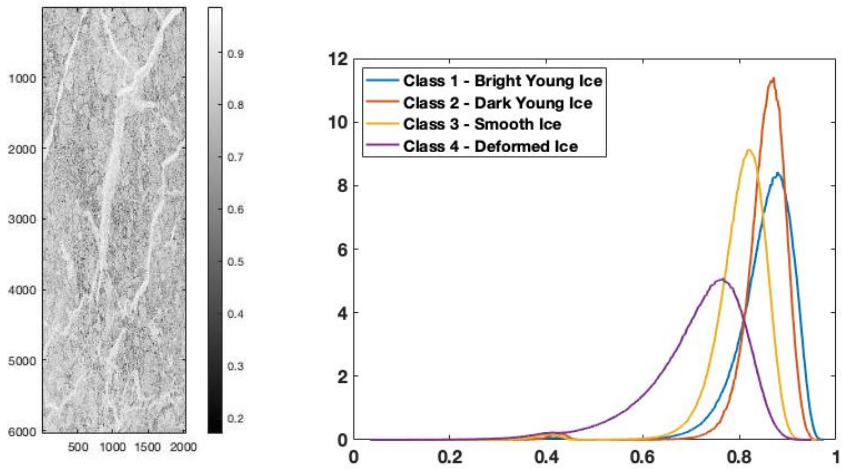

(a) **(b)**

Figure 7.13: Images taken at 12:43 UTC on 02.12.2019, with incidence angle 20^o, where a) is the grey level image of Degree of Polarization, and b) histograms of Degree of Polarization separated by classes.

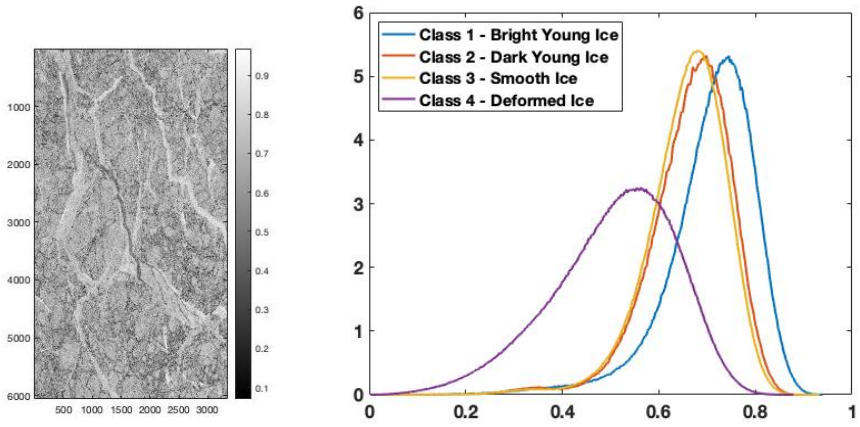

(a) **(b)**

Figure 7.14: Images taken at 06:03 UTC on 02.12.2019, with incidence angle 35^o, where a) is the grey level image of Degree of Polarization, and b) histograms of Degree of Polarization separated by classes.

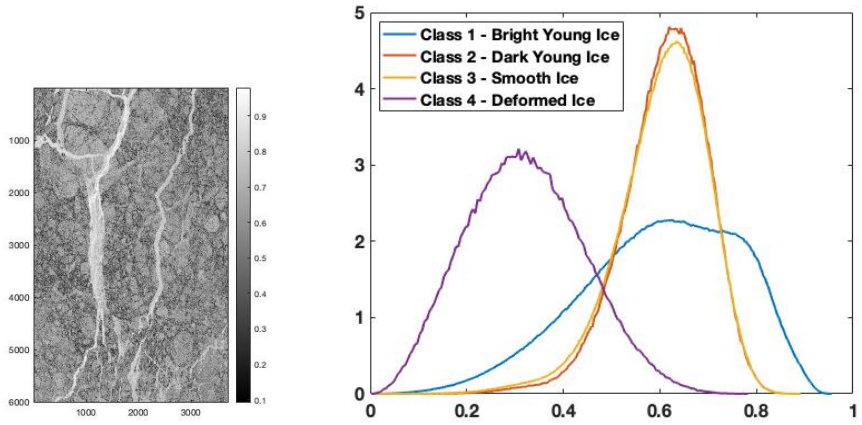

(a) (b)

Figure 7.15: Images taken at 14:23 UTC on 02.12.2019, with incidence angle 40^o, where a) is the grey level image of Degree of Polarization, and b) histograms of Degree of Polarization separated by classes.

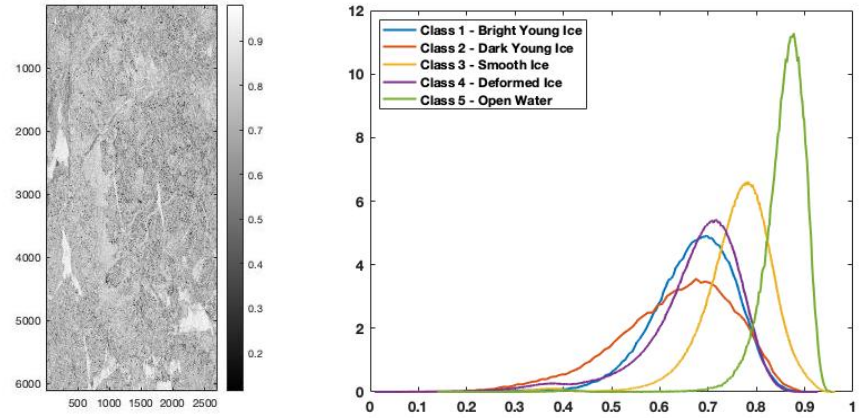

(a) (b)

Figure 7.16: Images taken at 13:25 UTC on 04.12.2019, with incidence angle 28^o, where a) is the grey level image of Degree of Polarization, and b) histograms of Degree of Polarization separated by classes.

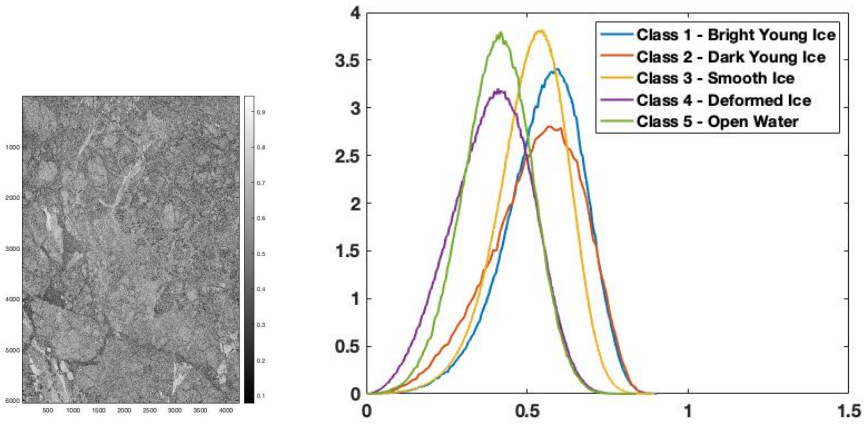

(a) **(b)**

Figure 7.17: Images taken at 15:05 UTC on 04.12.2019, with incidence angle 47^o, where a) is the grey level image of Degree of Polarization, and b) histograms of Degree of Polarization separated by classes.

It can be seen in Figures [7.13a, 7.14a and 7.15a] for data set 1 that the thinner sea ice types have higher values in data set 1. The DoP is a parameter that can be used to describe the roughness of the surface as described in section [6.2.3], and is therefore believed to be useful for separation of the deformed ice class from the other sea ice types. In the histograms in Figures [7.13b, 7.14b, 7.15b, 7.16b and 7.17b] it is possible to observe that the parameter can clearly separate the deformed ice class from the other sea ice types in data set 1. The type of scattering mechanism will have an impact on the values of the parameter, as for the deformed ice type more volume scattering will be expected. Looking at the results of the H/A/$\overline{\alpha}$ the areas believed to have a higher share of volume scattering corresponds well with the areas where there is deformed ice.

Moreover the incidence angle effect can be observed when comparing the images with lower incidence angles [Figures 7.13a and 7.16a] to those with higher incidence angles [Figures 7.15a and 7.17a], as the higher the incidence angle the lower the DoP values. This dependency is also demonstrated in Figure [7.18] where the mean value and standard deviation of the DoP (for data set 1) is plotted against incidence angles for the deformed ice and smooth ice classes. The DoP has lower values for the deformed ice, which is consistent with the definition from [Lee and Pottier, 2009] stating that the deformed ice will depolarize the signal and DoP $\rightarrow$ 0. From the results in Figure [7.18] it is possible to observe that the separability between deformed ice and smooth is is increasing with the increase of incidence angle. The fitted line is created as a visual effect connecting the points using *polyfit* in Matlab. Higher values of DoP indicates that the returning wave is still polarized and the surface being

smooth, which corresponds well with the higher values seen in the leads of data set 1.

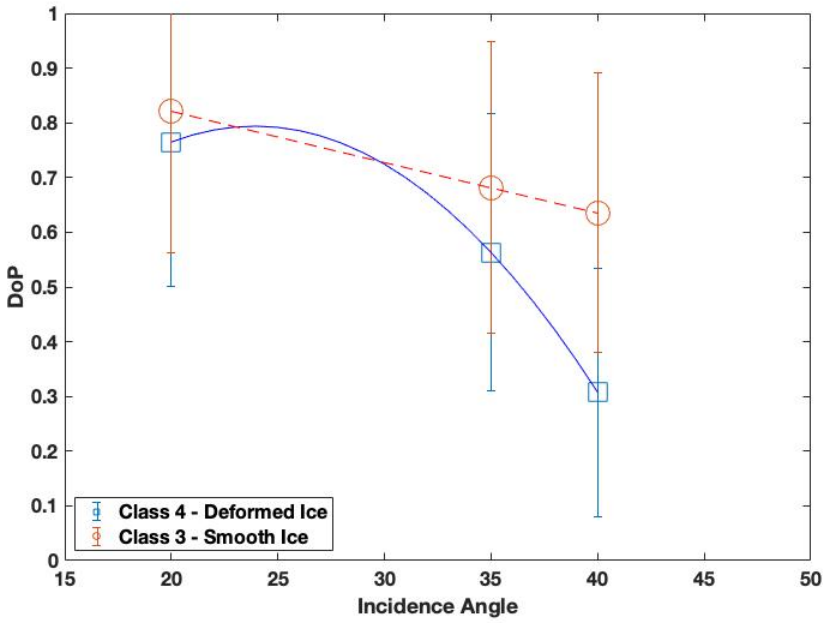

Figure 7.18: Mean and standard deviation of the DoP for data set 1 plotted against incidence angle for the deformed ice and smooth ice classes.

For data set 2 the deformed sea ice has low DoP values though there is less separability between any of the classes. As can be seen in [Espeseth et al., 2020] the DoP is affected by noise in the data, and as seen in the noise analysis performed in section [6.4] the SNR for multiple of the classes are close to the noise floor. With low SNR the DoP is expected to be approaching 0.5 (in case of assumed reciprocity) [Espeseth et al., 2020], and this is what can be observed in Figure [7.17b].

In summary the DoP can, provided sufficient SNR, be used to separate the deformed ice areas from the other sea ice types, but it is incidence angle dependent.

7.4 Polarimetric Coherence

The grey level images for the polarimetric coherence parameter are presented in Figures [7.19a, 7.20a and 7.21a] for data set 1 and Figures [7.22a and 7.23a]

for data set 2. Histograms for each image representing the individual classes are presented in Figures [7.19b, 7.20b and 7.21b] for data set 1 and Figures [7.22b and 7.23b] for data set 2.

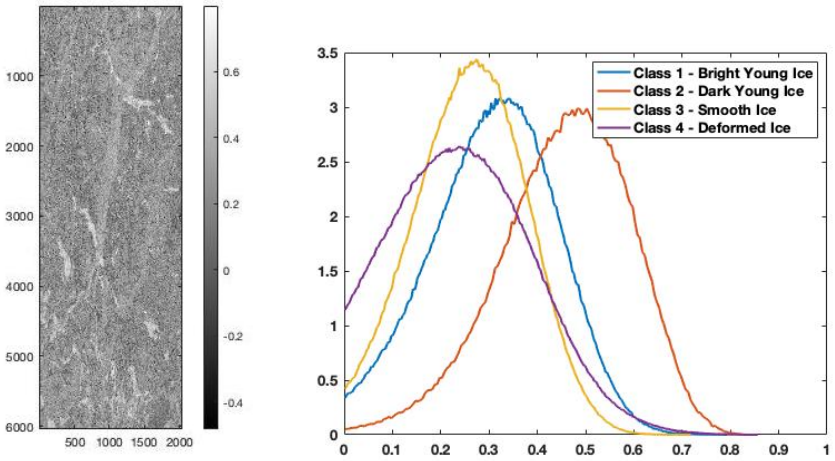

(a) **(b)**

Figure 7.19: Images taken at 12:43 UTC on 02.12.2019, with incidence angle 28^o, where a) is the grey level image of polarimetric coherence, and b) histograms of polarimetric coherence separated by classes.

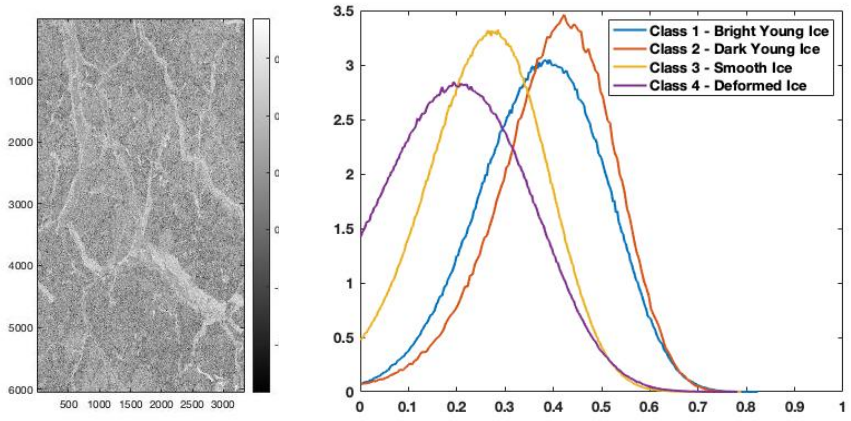

(a) **(b)**

Figure 7.20: Images taken at 06:03 UTC on 02.12.2019, with incidence angle 47^o, where a) is the grey level image of polarlimetric coherence, and b) histograms of polarimetric coherence separated by classes.

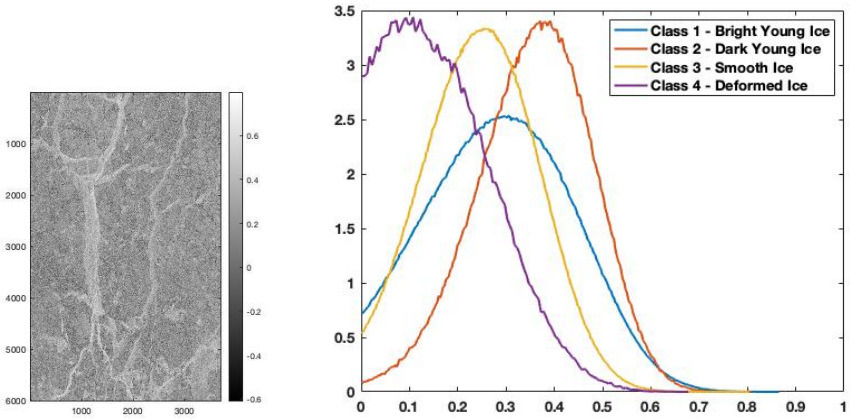

(a) **(b)**

Figure 7.21: Images taken at 14:23 UTC on 02.12.2019, with incidence angle 40^o, where a) is the grey level image of polarimetric coherence, and b) histograms of polarimetric coherence separated by classes.

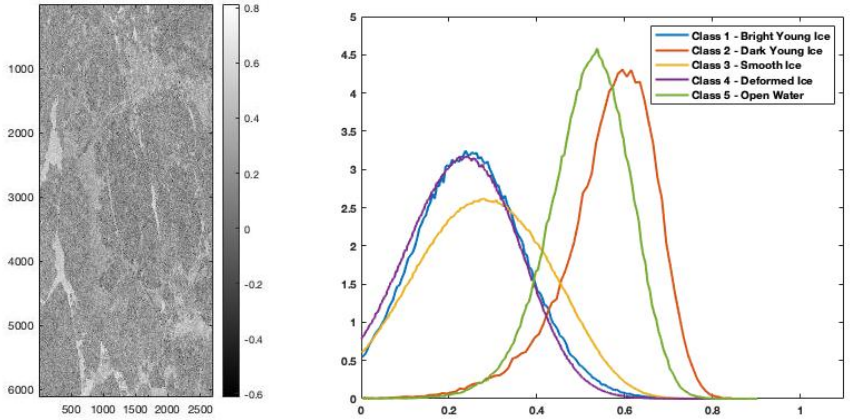

(a) **(b)**

Figure 7.22: Images taken at 13:25 UTC on 04.12.2019, with incidence angle 28^o, where a) is the grey level image of polarimetric coherence, and b) histograms of polarimetric coherence separated by classes.

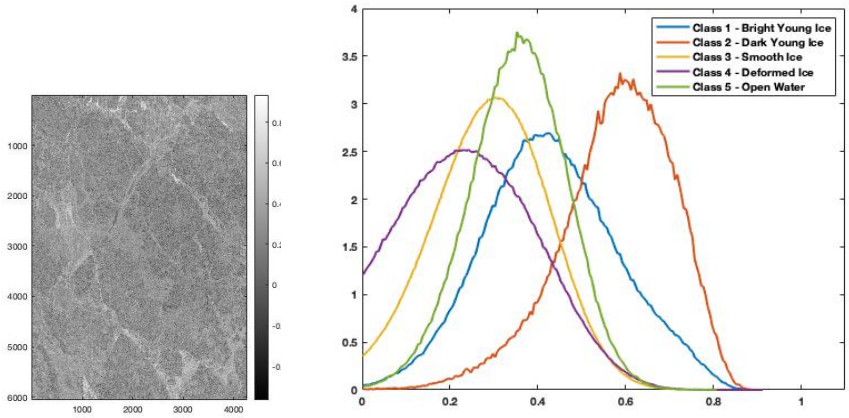

(a) **(b)**

Figure 7.23: Images taken at 15:05 UTC on 04.12.2019, with incidence angle 47^o, where a) is the grey level image of polarimetric coherence, and b) histograms of polarimetric coherence separated by classes.

The polarimetric coherence as described in section [6.2.4] is believed to be an indicator of surface roughness. Low values of the parameter means that the signal has been depolarized, and higher value means that the returning signal is polarized. Looking at the grey level images presented in Figures [7.19a, 7.20a, 7.21a, 7.22a and 7.23a] the high values of the parameter can be seen in the thin ice areas (leads), where the depolarization is expected to be low.

Looking at the histograms presented in Figures [7.19b, 7.20b and 7.21b] for data set 1, there is no clear separation between the sea ice classes in this data set. However, the deformed ice class has the lowest mean value in the images compared to the other sea ice classes. Also the thinner ice types (bright young ice and dark young ice) looks to have slightly higher values.

In data set 2, it can be observed (as for the other parameters as well) a large variation in the results. The grey level image for the lower incidence angle case (Figure [7.22a]) clearly shows higher values over the thin ice areas, while for the higher incidence angle case in Figure [7.23a] this is more diffuse. Analysing the histogram results in Figures [7.22b and 7.23b] it looks to be a large variation in the results. The open water class and dark thin ice class are well separated in the case with low incidence angle (Figure [7.22b]), but for the higher incidence angle the dark young ice is still well separated, but open water are more mixed with the other classes.

The polarimetric coherence does not appear to provide a good separability between the here studied sea ice classes, but can possibly be combined with

other parameters to extract extra information as the parameter e.g. has slightly lower values for the deformed ice.

7.5 Discussion Summary

A brief summary of the most important findings related to each polarimetric parameter that have been discussed in this chapter is presented in this section.

The co-polarization ratio is a good parameter to separate open water and young ice types from other sea ice types. The parameter is using both co-polarized channel, and as the cross-polarisation channels are not included have a better overall SNR. For the case without open water (data set 1) the separability between the thinner ice (bright young ice and dark young ice) look to be decreasing as the incidence angle increases. In data set 2 there is good separability in both cases, although the co-polarization values for open water seem to increase with increasing incidence angle.

Both the DoP and the M-parameter showed good ability to separate deformed ice from the other classes, and as the two parameter had an opposite effect from changing incidence angle, low incidence angle will give low M values and high DoP values and a high incidence angle will give high M values and low DoP values, a combination of these two parameters can be useful to further explore.

The polarimetric coherence is theoretically a good parameter for surface roughness, but as seen in the results the parameter did not display good separability between any of the classes. Although the values for deformed ice seems to be slightly lower than the rest, and may be possible to combine with another parameter for improved separability.

8

Conclusion and Future Work

As described in the introduction the Arctic regions of the Earth are largely covered by sea ice, and this sea ice have an important function on the Earth's climate system as well as the marine ecosystems.

8.1 Conclusion

The aim of this thesis was to investigate parameters extracted from fully polarimetric radar data and to see if it can be utilized for improved sea ice monitoring. The polarimetric parameters selected for this study were assessed to see if it is possible to provide additional information about the sea ice type and scattering mechanisms than what is possible using dual-polarization data, where the latter is is used in today's operational ice charts. The Radarsat-2 data used here were collected during a Nansen legacy cruise in December 2019 north of Svalbard and contains both new and older sea ice with different degrees of roughness.

The two main research questions presented in the introduction were:

1. *Is it possible to use the polarimetric parameters studied in this thesis to*

determine sea ice type?

2. *In the case of varying incidence angle, how does the parameters behave?Can the parameters be used without having to consider incidence angle?*

As an answer to the first question, three of the four polarimetric parameters studied showed promise in separating one or more sea ice classes from the other classes. The co-polarization ratio proves to be a good parameter to separate the thinner ice types (bright young ice and dark young ice) and open water from the rest of the ice classes (deformed ice and smooth ice). Both the DoP and the M-parameter have a good separability for the deformed ice class from the other ice types, which can be further explored since this is the thickest ice class. The polarimetric coherence did not show any good separability between the investigated classes, and could not be used individually to determine sea ice type for the images used in this study.

Looking at the second research question, one of the four polarimetric parameters appear to be independent of incidence angle changes, where the polarimetric coherence indicate no significant variations with varying incidence angles. The co-polarization ratio on the other hand seems to be dependent on the change of incidence angle, where the separability for the lower incidence angle case is better than for the higher incidence angles. In the case of open water seen in data set 2, the separability looks to be good for both high and low incidence angles. Both the DoP and M-parameter appear to be dependent on changing incidence angles, although the effect seems to be opposite where higher (lower) incidence angles will give high (low) values for the M-parameter and low (high) values for the DoP. So when using these polarimetric parameters, the incidence angle information needs to be considered when using DoP and M-parameter, but can be considered to a lesser degree for the co-polarization ratio and the polarimetric coherence.

8.2 Limitations

As seen in this thesis, and especially in the results for data set 2, noise may be a problem when studying low backscatter sea ice types. If the data has a too low SNR, often seen as SNR less than 10 dB, this can have an impact on the estimated polarimetric parameters studied in this thesis. In particular were the open water and dark young ice affected by a low SNR, which resulted in e.g. the DoP values to approach a value of 0.5, which was observed in [Espeseth et al., 2020] to be the value approached when the SNR was too low.

The number of data sets used in this study (2) might not be enough to fully conclude the effect of each polarimetric parameter used in this study. A larger study should be performed in order to confirm the results found.

8.3 Future Work

Some of the results and findings in this thesis would be interesting cases for future studies.

The first case is the negative co-polarization values observed for the thinner sea ice types. Why does some data sets display these values? It would be interesting to further investigate the data to see if a reason could be found. From this thesis there is a full data set with three separate images displaying this effect, which could be used in future studies.

Another interesting case to further explore is the relationship between DoP and the M-parameter. Since they are both separating the deformed ice class and also displaying opposite trends with changing incidence angle it could be useful to create a classifier combining these two parameters.

Bibliography

[IEE, 2003] (2003). Ieee standard letter designations for radar-frequency bands. *IEEE Std 521-2002 (Revision of IEEE Std 521-1984)*, pages 1–10.

[Brekke et al., 2014] Brekke, C., Holt, B., Jones, C., and Skrunes, S. (2014). Discrimination of oil spills from newly formed sea ice by synthetic aperture radar. *Remote Sens. Environ.*, 145:1–14.

[Campbell, 2011] Campbell, J. B. (2011). Introduction to remote sensing.

[Cloude, 2010] Cloude, S. (2010). Polarisation : applications in remote sensing.

[Doulgeris, 2013] Doulgeris, A. (2013). A simple and extendable segmentation method for multi- polarisation sar images. *POLinSAR 2013*, page 9.

[Doulgeris and Eltoft, 2010] Doulgeris, A. and Eltoft, T. (2010). Scale mixture of gaussian modelling of polarimetric sar data. *J. Appl. Signal Process.*, 874592.

[Drinkwater et al., 1992] Drinkwater, M. R., Kwok, R., Rignot, E., Israelsson, H., Onstott, R. G., and Winebrenner, D. P. (1992). *Potential Applications of Polarimetry to the Classification of Sea Ice*, chapter 24, pages 419–430. American Geophysical Union (AGU).

[ESA,] ESA. Polarimetric decompositions. `www.uat.esaportal.eu/documents/653194/656796/Polarimetric_Decompositions.pdf`. Accessed: 2018-11-30.

[Espeseth et al., 2020] Espeseth, M. M., Brekke, C., Jones, C. E., Holt, B., and Freeman, A. (2020). The impact of system noise in polarimetric sar imagery on oil spill observations. *IEEE Transactions on Geoscience and Remote Sensing*, 58(6):4194–4214.

[Geldsetzer and Yackel, 2009] Geldsetzer, T. and Yackel, J. (2009). Sea ice type and open water discrimination using dual co-polarized c-band sar.

Can. J. Remote. Sens., 35(1).

[Gill et al., 2013] Gill, J. P., Yackel, J. J., and Geldsetzer, T. (2013). Analysis of consistency in first-year sea ice classification potential of c-band sar polarimetric parameters. *Canadian Journal of Remote Sensing*, 39(2):101–117.

[Isleifson et al., 2010] Isleifson, D., Hwang, B., Barber, D. G., Scharien, R. K., and Shafai, L. (2010). C-band polarimetric backscattering signatures of newly formed sea ice during fall freeze-up. *IEEE Transactions on Geoscience and Remote Sensing*, 48(8):3256–3267.

[Jain et al., 1995] Jain, R., Kasturi, R., and Schunck, B. (1995). *Machine Vision*.

[Jin and Xu, 2013] Jin, Y. and Xu, F. (2013). *Polarimetric Scattering and SAR Information Retrieval*. Wiley - IEEE. Wiley.

[Johannessen et al.,] Johannessen, J., Collard, F., Chapron, B., Romeiser, R., and Alpers, W. Sar instrument principles and processing.

[Johansson et al., 2018] Johansson, A., Brekke, C., Spreen, G., and King, J. (2018). X-, c-, and l-band sar signatures of newly formed sea ice in arctic leads during winter and spring. *Remote Sensing of Environment*.

[Kinderaas, 2018] Kinderaas, I. (2018). Analysis of quadpol features of relevance for sea-ice classification. *Pilot Project*.

[Lee and Pottier, 2009] Lee, J.-S. and Pottier, E. (2009). *Polarimetric Radar Imaging : From basics to applications*.

[Leppäranta, 2011] Leppäranta, M. (2011). *The Drift of Sea Ice*. Springer Berlin Heidelberg.

[Lohse, 2021] Lohse, J. (2021). *On Automated Classification of Sea Ice Types in SAR Imagery*. PhD thesis.

[Lohse et al., 2020] Lohse, J., Doulgeris, A., and Dierking, W. (2020). Mapping sea-ice types from sentinel-1 considering the surface-type dependent effect of incidence angle. *Annals of Glaciology*, 61(83).

[Lubin and Massom, 2006] Lubin, D. and Massom, R. (2006). Polar remote sensing : Volume i: Atmosphere and oceans.

[Martinez and Byrnes, 2002] Martinez, A. and Byrnes, A. P. (2002). Mod-

eling dielectric-constant values of geologic materials: An aid to ground-penetrating radar data collection and interpretation. *Current Research in Earth Sciences*, 247.

[MET.no,] MET.no, M. I. Oppdaterte iskart fra istjenesten.

[Moen, 2015] Moen, M.-A. (2015). Analysis and interpretation of c-band polarimetric sar signatures of sea ice.

[Mott, 2006] Mott, H. (2006). *Remote Sensing with Polarimetric Radar*. John Wiley Sons, Inc., Hoboken, NJ, USA.

[Shokr and Sinha, 2015] Shokr, M. and Sinha, N. (2015). *Sea Ice: Physics and Remote Sensing*. Geophysical Monograph Series. Wiley.

[Souyris et al., 2007] Souyris, J.-C., Stacy, N., Ainsworth, T., Lee, J.-S., and Dubois-Fernandez, P. (2007). Sar compact polarimetry (cp) for earth observation and planetology: Concepts and challenges. pages 17–.

[Stroeve et al., 2012] Stroeve, J., Markus, T., Meier, W., and Miller, J. (2012). The arctic's rapidly shrinking sea ice cover: a research synthesis. *Climate Change*, 110:1005–1027.

[Tucker III et al., 1992] Tucker III, W. B., Perovich, D. K., Gow, A. J., Weeks, W. F., and Drinkwater, M. R. (1992). *Physical Properties of Sea Ice Relevant to Remote Sensing*, chapter 2, pages 9–28. American Geophysical Union (AGU).

[Ulaby and Elachi, 1990] Ulaby, F. and Elachi, C. (1990). *Radar Polarimetry for Geoscience Applications*. Artech House remote sensing library. Artech House.

[van Zyl and Kim, 2011] van Zyl, J. and Kim, Y. (2011). *Synthetic Aperture Radar Polarimetry*. JPL Space Science and Technology Series. Wiley.

[WMO, 2010] WMO, W. M. O. (2010). *WMO-No 574:Sea-ice information services in the world*.